

Bifurcation control for a ship maneuvering model with nonsmooth nonlinearities

Miriam Steinherr Zazo* Jens D. M. Rademacher†

June 26, 2022

Abstract

We consider a widely used form of models for ship maneuvering, whose nonlinearities entail continuous but nonsmooth second-order modulus terms. For such models bifurcations of straight motion are not amenable to standard center manifold reduction and normal forms. Based on a recently developed analytical approach, we nevertheless determine the character of local bifurcations when stabilizing the straight motion course with standard proportional control. For a specific model class we perform a detailed analysis of the linearization to determine the location of these bifurcations in the control parameter space and its dependence on selected design parameters. By computing the analytically derived characteristic parameters, we find that ‘safe’ supercritical Andronov–Hopf bifurcations are typical. Through numerical continuation we provide a more global bifurcation analysis, which identifies the arrangement and relative location of stable and unstable equilibria and periodic orbits.

Key words: Stability, Nonsmoothness, Hopf Bifurcation, Lyapunov Coefficient

AMS subject classifications: 34H15, 34H20, 37N35, 93D20

1 Introduction

A typical task in ship maneuvering is to maintain a specified heading. In standard differential equation models for ship maneuvering such straight motion appears as an equilibrium point. We consider here the frequent situation in which this is unstable in absence of control, and study the effectiveness of a standard proportional control to stabilize it. We do not specifically design the control for this task, which would be a broader goal in bifurcation control [1, 6, 11]. Instead, we identify the possibility to stabilize the straight motion in terms of the given control gains. Our main interest lies in the resulting nonlinear effects. The given control combines the steering angle η with the yaw angle ψ , where $\psi = 0$ is the desired heading, and the yaw velocity $r = \dot{\psi}$.

*University of Bremen, Germany, Department 3 – Mathematics, m.steinherr@uni-bremen.de

†University of Bremen, Germany, Department 3 – Mathematics, jdmr@uni-bremen.de

The standard proportional yaw damping and yaw restoring control takes the form $\eta = \varepsilon_r r + \varepsilon_\psi \psi$ with control gains ε_r and ε_ψ [13, 17, 20]. Stabilization on a linear level identifies gain margins at which linear growth rates of perturbations switch from positive to negative [13]. These gain margins form a stability boundary curve in the control parameter plane.

It turns out that for the selected model class the crossing from the unstable to the stable region is either a pitchfork or an Andronov–Hopf bifurcation. It is well known that these bifurcations are generically either subcritical or supercritical [5]. For a subcritical bifurcation, the linearly stable state co-exists with a nearby unstable bifurcated state, i.e., the effect of bifurcation is inside the stable region in control parameter space. Although linear analysis predicts stability, the basin of attraction can be very small. When random perturbations exceed this small basin, local information is insufficient to determine how the system further evolves. For a supercritical bifurcation, the unstable state co-exists with a stable bifurcated state before parameters have reached the stable region. In this case the linear stability boundary is a safe estimate for stabilization. It is therefore important to be able to determine whether the bifurcation in a control scenario is supercritical or subcritical [13].

The criticality can be inferred from the so-called first Lyapunov coefficient for the Hopf bifurcation or its analogue for the pitchfork bifurcation. If the nonlinear terms are smooth, then this coefficient can be computed by means of a center manifold reduction and normal form analysis [5]. We refer to [1, 6, 10] and the references therein for studies in the context of smooth ship models and their relation to bifurcation control. We also mention that various studies have numerically investigated bifurcations and the resulting branches of solutions for smooth models of ship maneuvering without focus on the Lyapunov coefficient [14, 15, 16, 20]. However, the standard class of models for ship maneuvering that we consider features nonlinearities with continuous nonsmooth terms [2, 3, 4, 8, 17, 21, 22]. Here the smooth theory is not applicable in general. In [17], a purely numerical study of bifurcations for such a model is presented, which avoids the problem and does not determine Lyapunov coefficients.

Originally motivated by these ship models, we have developed a theoretical framework that admits to derive the first Lyapunov coefficient for a broad class of continuous nonsmooth models [18]. The main purpose of the current paper is to illustrate the application of this theory to models of ship maneuvering. As a preparatory part for this nonlinear analysis, but of independent interest, we provide a detailed analytical study of stability boundaries for the selected model class. This provides explicit formulas for stability boundaries in terms of the control gains and ship design parameters. In particular, the location of the propulsion force on the hull has an important impact on the geometry and location of the stability boundary. Concerning criticality of bifurcations, we find that in the considered models all are supercritical and thus safe. In order to gain additional insight into the arrangement of the bifurcating periodic orbits more globally in control parameter space, we perform numerical continuation studies. Some of the bifurcating solutions have broadly varying yaw angle, so that for their study we need to account for the global cylindrical topology of phase space. We find that the continuation of these periodic solutions and those from the Hopf bifurcation terminate in heteroclinic bifurcations that involve the cylindrical geometry.

This paper is structured as follows. We present a brief background regarding marine craft hydrodynamics in §2. Here we also present the specific equations of motion for the ship model

considered in this paper and detail the kind of control used. In the main section §3, we theoretically investigate the stability of the straight line motion and bifurcations from it. Included in this analysis is the impact of some ship design parameters. The numerical bifurcation and continuation analysis is presented in §4, illustrating the preceding theoretical study. For the continuation of solutions that have widely varying yaw angle, the control law is modified to depend periodically on the yaw angle. We show selected periodic orbits in phase space as well as the corresponding ship tracks in Earth-fixed coordinates. Finally, in §5 we discuss the results and present possible directions for further research.

2 Model Equations and Background

Here we briefly discuss ingredients that are most relevant for our subsequent analysis. The kinetics is based on Newton’s second law and Euler’s axiom. With these, the rigid-body equations of motion take the form $\mathbf{M}\dot{\mathbf{v}} = \mathbf{F}(\mathbf{v})$, where \mathbf{v} is the vector of ship-fixed velocities and $\dot{\mathbf{v}}$ its time derivative. The matrix \mathbf{M} contains the mass coefficients, which include the added mass due to the water displacement and moments of inertia. The vector \mathbf{F} contains the forces from the hull, rudder, propeller and hydrodynamics, as well as the Coriolis term. Detailed derivations of the equations of motion for a marine craft can be found in, e.g., [8].

In the modeling of the hydrodynamic forces, we are interested in the nature of the arising nonlinear terms since their nonsmooth character is decisive in the analysis of bifurcations. One approach to the nonlinear terms follows the drag equation for high Reynolds number given by

$$F_D = -\frac{1}{2}\rho C_D A u |u|,$$

where u is the velocity of the body, ρ the density of the water, C_D the drag coefficient, and A the effective drag area, [8]. This equation is a consequence of (I) the experimental observation that the drag force $F_D = F_D(\rho, A, u)$ is a function of ρ, A, u ; (II) the fact that, as an opposing force, F_D must be odd with respect to u ; and (III) that dimensional analysis in a power law ansatz $F_D = \rho^\alpha A^\beta u^\gamma C$ for $u > 0$ with exponents $\alpha, \beta, \gamma \in \mathbb{R}$ and a constant C , implies $\alpha = \beta = 1$, $\gamma = 2$. Indeed, polynomial regression studies on the representation of hydrodynamic forces confirm that $u|u|$, $v|v|$, $r|r|$ and the mixed terms $v|r|$, $r|v|$, are the relevant higher-order terms [23, 24]. These *second-order modulus terms* can be regarded as square law damping in this context. In addition, these nonlinear terms can be motivated by a Taylor expansion to second-order, where the absolute value is used to correct the signs [3]. Ship models with third-order Taylor approximations are also used in the literature, e.g., [12, 15, 20]. However, when it comes to bifurcation analysis, there is a significant difference between the second-order modulus and cubic terms as discussed in detail in [18] and reflected in our bifurcation analysis of §3.3.

The specific model equations that we will investigate are a variation of the 3 degree-of-freedom model from [3, 22], for which some basic analysis was conducted in [4]. The model parameters stem from the ‘Hamburg Test Case’ (HTC) characteristics, that we collect in Appendix A as needed. We adopt these values throughout, except when analyzing the impact of selected parameter changes. The general dimensional 3 degree-of-freedom model takes the

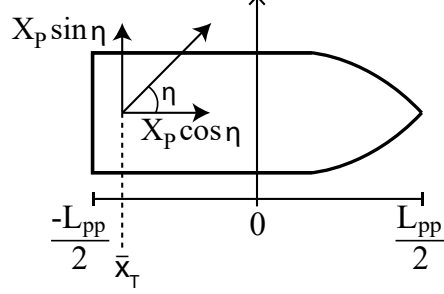


Figure 1: Sketch of a ship model illustrating the location of the thruster and the thruster force components for the surge, $X_P \cos \eta$, and the sway, $X_P \sin \eta$.

form

$$\begin{pmatrix} \bar{m} + \bar{m}_{uu} & 0 & 0 \\ 0 & \bar{m} + \bar{m}_{vv} & \bar{m}_{vr} \\ 0 & \bar{m}_{rv} & \bar{I}_z + \bar{m}_{rr} \end{pmatrix} \begin{pmatrix} \dot{u} \\ \dot{v} \\ \dot{r} \end{pmatrix} = \begin{pmatrix} \bar{m}vr + X \\ -\bar{m}ur + Y \\ N \end{pmatrix}, \quad (2.1)$$

where u, v and r are the surge, sway and yaw velocities, respectively. The external forces X, Y, N for the ‘rudder model’ of [22] are of the form $X = X_H + X_R + X_P$, $Y = Y_H + Y_R$, $N = N_H + N_R$ with the contributions from the hull (H), the rudder (R) and the propeller (P) of the vessel.

In order to facilitate the presentation of the mathematical method and analysis, we combine the rudder and propeller forces as in [4] into a simpler ‘thruster force’, which gives

$$X = X_H + X_P \cos \eta, \quad Y = Y_H + X_P \sin \eta, \quad N = N_H + \bar{x}_T X_P \sin \eta. \quad (2.2)$$

The thruster acts on the hull at a longitudinal position $\bar{x}_T \in [-\frac{1}{2}L_{pp}, \frac{1}{2}L_{pp}]$, measured from the midship of the marine craft towards the front, and exerts a propulsion force in the steering direction η of amplitude given by the propeller force X_P ; see Fig. 1. This is similar to the rudder force in [17], where X_P is constant while we will consider nonlinear X_P . The variable η represents the rudder angle and is an external input, which will be assumed to obey a specific control law design.

For the hull forces we take the general non-dimensional form of [3, 22]. Compared to (2.1), we scale u, v by the ship length L_{pp} to unit 1/s; the full non-dimensionalization follows below. With $V = \sqrt{u^2 + v^2}$, the forces read

$$\begin{aligned} X_H &= X_{u|u}|u|^2 + X_{\beta\gamma}vr, \\ Y_H &= Y_{\beta}uv + Y_{\gamma}ur + Y_{\beta|\beta}|v||v| + Y_{\gamma|\gamma}|r||r| + Y_{\beta|\gamma}|v||r| + Y_{|\beta|\gamma}|v||r| + Y_{abu^3}|v|vV^{-3}, \\ N_H &= N_{\beta}uv + N_{\gamma}ur + N_{u'\gamma c}u|r|rV^{-1} + N_{\gamma|\gamma}|r||r| + N_{\beta|\beta}|v||v| \\ &\quad + N_{\beta\beta\gamma}rv^2V^{-1} + N_{\beta\gamma\gamma}vr^2V^{-1} + N_{abu^3}v^3V^{-2}. \end{aligned}$$

To ease the exposition, some exponents of terms in Y_H and N_H are already specified to the HTC from which we choose as default all values of coefficients; see Appendix A. Several nonlinear terms in these forces implement the aforementioned second-order modulus form of the drag analogous to [3, 8, 17]. The corresponding non-dimensionalization, up to time, of (2.1) has the

same form, but with the dimensionless mass coefficients listed in Table 1. Within N the thruster position turns into the dimensionless $x_T \in [-1/2, 1/2]$. As default value we take the rudder position of the HTC, which gives $x_T \approx -0.49$; see [22].

The propeller force taken from [22] in the corresponding scaling reads

$$X_P = 2(1-t) \frac{L_{PP}}{T} n_p^2 D_p^4 K_T, \quad K_T := \sum_{i=0}^5 K_{Ti} \left(\frac{1-w}{n_p D_p} u \right)^i, \quad (2.3)$$

where $n_p > 0$ is the propeller frequency, $D_p := \bar{D}_p / L_{PP}$ is the non-dimensional propeller diameter, and all other parameters are by default those of the HTC; see Appendix A. The propeller frequency can be removed by a non-dimensionalization of time. Indeed, all forces scale quadratically with respect to the velocity $u = n_p \check{u}$, e.g., $X_P = n_p^2 \check{X}_P(\check{u})$ with \check{X}_P independent of n_p . This implies the natural relation that all velocities are proportional to the propeller speed: rescaling all velocities and time proportional to n_p gives a factor n_p^2 on both sides of (2.1) so that n_p is removed upon division. Concerning the (dimensionless) propeller diameter D_p , we observe that scaling $u = D_p \tilde{u}$ gives $X_P = D_p^4 \tilde{X}_P(\tilde{u})$, where \tilde{X}_P is independent of D_p . However, not all forces scale in the same way and, as we will explain below, the value of D_p enters into the analysis of the model. In the remainder of this paper, we discuss the fully non-dimensional equations using the same notation and fixing $n_p = 1$ in (2.3).

The model is completed by the control law for the steering angle η . Here we choose a standard combination $\eta = \eta_1 + \eta_2$ of yaw damping proportional control (P-control) η_1 and yaw restoring P-control η_2 ; we refer to [8] for a general background. The first consists of adding a proportional compensation to the yaw velocity r by setting $\eta_1 = \varepsilon_r(r - r_*)$, with target yaw velocity r_* and control parameter $\varepsilon_r \geq 0$. Analogously, for the yaw angle ψ we have $\eta_2 = \varepsilon_\psi(\psi - \psi_*)$ with target yaw angle ψ_* and second control parameter $\varepsilon_\psi \geq 0$. Notably, for $\varepsilon_\psi > 0$ this requires to add $\dot{\psi} = r$ as a fourth equation to (2.1). The control parameters $\varepsilon_r, \varepsilon_\psi \geq 0$ are also referred to as control gains. For controlling a straight line trajectory, we have $r_* = 0$ and, since (2.1) is otherwise independent of ψ , we may set $\psi_* = 0$. This gives

$$\eta = \varepsilon_r r + \varepsilon_\psi \psi, \quad (2.4)$$

which is a standard P-controller that also appears in, e.g., [13, 17, 20].

In the following we study the non-dimensional 4D ‘thruster model’

$$\begin{pmatrix} m + m_{uu} & 0 & 0 & 0 \\ 0 & m + m_{vv} & m_{vr} & 0 \\ 0 & m_{rv} & I_z + m_{rr} & 0 \\ 0 & 0 & 0 & 1 \end{pmatrix} \begin{pmatrix} \dot{u} \\ \dot{v} \\ \dot{r} \\ \dot{\psi} \end{pmatrix} = \begin{pmatrix} mvr + X_H + \tau(u) \cos \eta \\ -mur + Y_H + \tau(u) \sin \eta \\ N_H + x_T \tau(u) \sin \eta \\ r \end{pmatrix}, \quad (2.5)$$

where we denote $\tau(u) := X_p$ for later convenience. For $\varepsilon_\psi = 0$ we also consider the 3D reduction to the invariant (u, v, r) -subsystem, i.e., the non-dimensionalized form of (2.1). It turns out to be relevant that the propeller force is monotone decreasing in the surge $u > 0$, i.e.,

$$\partial_u \tau(u) < 0. \quad (2.6)$$

This is equivalent to $\partial_u K_T < 0$ for the HTC since in (2.3) we have $t, w < 1$. The fact that $\partial_u K_T < 0$ holds for $u > 0$ is not obvious, but it can be verified numerically for the HTC.

We write (2.5) more compactly as $M\dot{\mathbf{v}} = F(\mathbf{v})$, where M is the matrix on the left hand side of (2.5), containing the non-dimensionalized mass matrix from (2.1), $F(\mathbf{v})$ is the right hand side, and $\mathbf{v} = (u, v, r, \psi)^\top$. Since M is invertible, the equivalent explicit compact form of (2.5) reads

$$\dot{\mathbf{v}} = M^{-1}F(\mathbf{v}). \quad (2.7)$$

3 Theoretical Analysis

In this section, we analyze the impact of the yaw damping and yaw restoring control (2.4) on the stability and bifurcation of the equilibrium straight motion. We include variations of the selected design parameters D_p , the propeller diameter, and x_T , the thruster position, in order to illustrate the methodology. We start discussing the existence of the straight motion as an equilibrium in the ship-fixed coordinates, then turn to the linear stability, and finally analyze the resulting bifurcations.

3.1 Equilibrium Straight Motion

The straight motion of the ship with constant speed corresponds to an equilibrium point given by $(u_0, v_0, r_0, \psi_0) = (u_0, 0, 0, 0)$, with $u_0 > 0$ and the reference direction $\psi_0 = 0$ of system (2.5). Equilibria are those $\mathbf{v} = (u, v, r, \psi)^\top$ for which $F(\mathbf{v})$ in (2.7) vanishes. Setting $v = r = \psi = 0$, the last three components of $F(\mathbf{v})$ become zero, which in fact holds for any ψ_0 if $\varepsilon_\psi = 0$, so that in this case we obtain a line of equilibrium motion in any direction. For $\varepsilon_\psi \neq 0$, this is constrained to the reference direction $\psi_0 = 0$. The remaining first component of $F(\mathbf{v})$ now reads $X_H + \tau(u)\cos(0)$, which gives the condition for the equilibrium straight velocity u_0 as

$$X_{u|u}u_0^2 + \tau(u_0) = 0, \quad (3.1)$$

independent of the control parameters $\varepsilon_r, \varepsilon_\psi$. This equation possesses a unique positive solution if (2.6) holds, i.e., $\partial_u \tau(u) < 0$, since $\tau(0) > 0$ and $X_{u|u} < 0$, and therefore the left hand side is strictly decreasing for $u > 0$. These conditions hold for the HTC values (see Appendix A), and then $u_0 = u_0^{\text{HTC}} \approx 0.03$ solves (3.1) uniquely. It also follows from (3.1) that $\tau(u_0) > 0$.

Regarding D_p and x_T , the equilibrium location is independent of x_T since this does not appear in (3.1). For the propeller diameter D_p , we scale $u = D_p \tilde{u}$ and $\tilde{\tau}(\tilde{u}) := D_p^{-4} \tau(D_p \tilde{u})$, which is independent of D_p . Then (3.1) becomes $X_{u|u} \tilde{u}_0^2 + D_p^2 \tilde{\tau}(\tilde{u}_0) = 0$, where the first addend is independent of D_p . Hence, the equilibrium depends on D_p , but for large values its location is approximately proportional to D_p . Indeed, the rescaled (3.1), upon multiplication by $(D_p^2 X_{u|u})^{-1}$, takes the form

$$D_p^{-2} \tilde{u}_0^2 + C_0 + P(\tilde{u}_0) = 0, \quad (3.2)$$

with $P(\tilde{u}_0) := C_1 \tilde{u}_0 + \dots + C_5 \tilde{u}_0^5$, where the C_i are real constants. In the limit $D_p \rightarrow \infty$, the term $D_p^{-2} \tilde{u}_0^2$ vanishes, and \tilde{u}_0 converges to the unique positive solution \tilde{u}_0^* of $C_0 + P(\tilde{u}_0) = 0$,

which is independent of D_p . Since $u = D_p \tilde{u}$, it follows that $u_0 \approx D_p \tilde{u}_0^*$ for $D_p \gg 1$. Condition (2.6) is readily verified numerically for any D_p ; for large D_p we can also see this rigorously by inspecting the expression for $\partial_u \tau(u_0)$ as a function of D_p , which reads

$$\partial_u \tau(u_0)(D_p) = \tilde{C}_5 D_p^3 \left(-\tilde{C}_4 \left(\frac{u_0}{D_p} \right)^4 + \tilde{C}_3 \left(\frac{u_0}{D_p} \right)^3 - \tilde{C}_2 \left(\frac{u_0}{D_p} \right)^2 + \tilde{C}_1 \frac{u_0}{D_p} - \tilde{C}_0 \right).$$

Here all \tilde{C}_i are positive constants. Thus, for u_0 exactly proportional to D_p we have $\partial_u \tau(u_0)(D_p) = -\tilde{C} D_p^3$, with $\tilde{C} > 0$, and the approximate proportionality implies $\partial_u \tau(u_0) < 0$ for $D_p \gg 1$.

3.2 Stability of Straight Motion

We first recall from [4] that the straight motion without control is linearly unstable. Indeed, $F'(\mathbf{v})$ from (2.7) at $\mathbf{v} = (u_0, 0, 0, 0)^\top$ reads

$$J := \begin{pmatrix} 2X_{u|u}u_0 + \partial_u \tau(u_0) & 0 & 0 & 0 \\ 0 & Y_\beta u_0 & (Y_\gamma - m)u_0 + \tau(u_0)\varepsilon_r & \tau(u_0)\varepsilon_\psi \\ 0 & N_\beta u_0 & N_\gamma u_0 + x_T \tau(u_0)\varepsilon_r & x_T \tau(u_0)\varepsilon_\psi \\ 0 & 0 & 1 & 0 \end{pmatrix}.$$

At $\varepsilon_\psi = 0$ it has vanishing fourth column, and hence, a zero eigenvalue, which is the same for $M^{-1}J$. The remaining eigenvalues of $M^{-1}J$ are those of its upper left 3×3 -submatrix, which we denote by S . This has block structure with upper left entry $\lambda_1 = (2X_{u|u}u_0 + \partial_u \tau(u_0))/(m + m_{uu})$, which is always negative since $X_{u|u}u_0 < 0$ and $\partial_u \tau(u_0) < 0$, as discussed above. Thus, the linear stability of the equilibrium point $(u_0, 0, 0)$ is determined by the lower right 2×2 -submatrix of S . For the HTC, and at $\varepsilon_r = 0$, we readily find that its eigenvalues are non-zero with opposite signs; cf. [4]. Due to the second-order modulus terms, the nonlinear terms in F are differentiable at $v = r = 0$, but not in a neighborhood of this. However, (2.7) can be cast as a semi-linear ordinary differential equation since $F(\mathbf{v}) = J\mathbf{v} + h(\mathbf{v})$, where $h(\mathbf{v}) = \mathcal{O}(\|\mathbf{v}\|^2)$. Therefore, the linear stability principle applies; see also [18]. Hence, the straight motion is unstable for the HTC without control and the free parameters D_p, x_T do not change this instability: x_T does not influence the stability analysis since the matrix and equilibrium do not depend on it, and the propeller diameter D_p enters only in $\partial_u \tau(u_0)$, which modifies the eigenvalue λ_1 of S , but – as noted above – it is negative for any value of D_p .

In the remainder of this section, we analyze the eigenvalues of $M^{-1}J$ when including the P-control (2.4). With $p_{11} = \lambda_1$, it has the form

$$A := M^{-1}J = \begin{pmatrix} p_{11} & 0 & 0 & 0 \\ 0 & p_{22} & p_{23} & p_{24} \\ 0 & p_{32} & p_{33} & p_{34} \\ 0 & 0 & 1 & 0 \end{pmatrix}, \quad (3.3)$$

and we write the other matrix entries as follows, noting the dependencies on $u_0, \varepsilon_\psi, \varepsilon_r$:

$$\begin{aligned}
p_{22} &= p_{22u}u_0, & p_{23} &= p_{23u}u_0 + q_{23}\tau(u_0)\varepsilon_r, & p_{24} &= q_{23}\tau(u_0)\varepsilon_\psi, \\
p_{32} &= p_{32u}u_0, & p_{33} &= p_{33u}u_0 + q_{33}\tau(u_0)\varepsilon_r, & p_{34} &= q_{33}\tau(u_0)\varepsilon_\psi,
\end{aligned}$$

with $D := (m + m_{vv})(I_z + m_{rr}) - m_{rv}m_{vr}$, and

$$\begin{aligned}
p_{22u} &= D^{-1}((I_z + m_{rr})Y_\beta - m_{vr}N_\beta), & p_{32u} &= D^{-1}(-m_{rv}Y_\beta + (m + m_{vv})N_\beta), \\
p_{23u} &= D^{-1}((I_z + m_{rr})(Y_\gamma - m) - m_{vr}N_\gamma), & q_{23} &= D^{-1}(I_z + m_{rr} - m_{vr}x_T), \\
p_{33u} &= D^{-1}(-m_{rv}(Y_\gamma - m) + (m + m_{vv})N_\gamma), & q_{33} &= D^{-1}(-m_{rv} + (m + m_{vv})x_T).
\end{aligned}$$

Further we define the following coefficients, which enter in the stability result:

$$\begin{aligned}
K_{11} &= q_{33}^2\tau(u_0)^2, \\
K_{02} &= q_{33}(p_{32u}q_{23} - p_{22u}q_{33})u_0\tau(u_0)^2, \\
K_{01} &= [(p_{22u} + p_{33u})(p_{32u}q_{23} - p_{22u}q_{33}) + q_{33}(p_{23u}p_{32u} - p_{22u}p_{33u})]u_0^2\tau(u_0), \\
K_{10} &= [(p_{22u} + p_{33u})q_{33} + p_{32u}q_{23} - p_{22u}q_{33}]u_0\tau(u_0), \\
K_{00} &= (p_{22u} + p_{33u})(p_{23u}p_{32u} - p_{22u}p_{33u})u_0^3.
\end{aligned} \tag{3.4}$$

With these preparations we can formulate our main result concerning the change of stability of the unstable straight motion equilibrium for the HTC values. This is a refinement of the result in [19], and implies ‘global controllability’ of the straight motion. This means that stabilization by the P-control is possible along any direction in the control parameter space, i.e., the positive quadrant of the $(\varepsilon_r, \varepsilon_\psi)$ -plane. In §3.2.1 we will find that this remains valid for any $D_p > 0$, and in §3.2.2 we will study the non-trivial impact of x_T .

By stabilization of the straight motion we mean exponential asymptotic stability, up to symmetry in ψ for $\varepsilon_\psi = 0$, of the equilibrium $(u, v, r, \psi) = (u_0, 0, 0, 0)$ in (2.5). Due to the linear stability principle this is equivalent to strictly negative real parts of the eigenvalues of A , or its 3D reduction S for the case $\varepsilon_\psi = 0$.

Theorem 3.1. *Consider the thruster model (2.5) with the HTC values and define*

$$\varepsilon_\psi(\varepsilon_r) := -\frac{K_{02}\varepsilon_r^2 + K_{01}\varepsilon_r + K_{00}}{K_{11}\varepsilon_r + K_{10}}, \tag{3.5}$$

with K_{ij} from (3.4) and $\varepsilon_r, \varepsilon_\psi$ the P-control parameters from (2.4). Fix any $\underline{\varepsilon}_r, \underline{\varepsilon}_\psi \geq 0$ and for $s \geq 0$ consider control parameters on the ray $s \cdot (\underline{\varepsilon}_r, \underline{\varepsilon}_\psi)$. Then, as s increases, the equilibrium $(u_0, 0, 0, 0)$ of (2.5) is stabilized when $s \cdot (\underline{\varepsilon}_r, \underline{\varepsilon}_\psi)$ crosses the curve defined by (3.5). This crossing point lies at a unique $s^* > 0$ for each fixed $\underline{\varepsilon}_r, \underline{\varepsilon}_\psi$. The eigenvalues of A behave as follows: for $\underline{\varepsilon}_\psi > 0$, a complex pair of eigenvalues traverses the imaginary axis as s crosses s^* , while for $\underline{\varepsilon}_\psi = 0$ one eigenvalue is fixed at zero and a simple real eigenvalue traverses zero at $s = s^*$.

The theorem states that the curve defined by (3.5) is a stability boundary for the control parameters, which is sometimes referred to as gain margin, e.g., [13]. We plot this stability boundary in Fig. 2, and illustrate the organization of the eigenvalues of A in the positive quadrant of the $(\varepsilon_r, \varepsilon_\psi)$ -plane. This eigenvalue configuration at $\varepsilon_\psi = 0$ and ε_r on the stability boundary

is reminiscent of a Bogdanov–Takens point. However, unlike a generic unfolding, for $\varepsilon_\psi = 0$ the right-hand side of (2.7) is independent of ψ so that $(u, v, r, \psi) = (u_0, 0, 0, \psi)$ with arbitrary ψ forms a line of equilibria. We discuss aspects of the resulting bifurcations in §3.3.1 and §4. The Hopf bifurcation analysis on the stability boundary for $\varepsilon_\psi > 0$ will be presented in §3.3.2. For the nonsmooth system, this analysis is more delicate than usual.

Proof. We analyze the eigenvalues of the linear part of (2.5) given by A in (3.3). As noted above, $p_{11} < 0$ for the HTC values, so that it suffices to consider the lower right 3×3 -matrix, which we denote by P . Its characteristic polynomial reads

$$Q_P(\lambda) = \det(\lambda I - P) = \lambda^3 + c_2\lambda^2 + c_1\lambda + c_0, \quad (3.6)$$

with I the 3-by-3 identity matrix and

$$\begin{aligned} c_0 &= p_{34}p_{22} - p_{24}p_{32} = (p_{22u}q_{33} - p_{32u}q_{23})u_0\tau(u_0)\varepsilon_\psi, \\ c_1 &= p_{22}p_{33} - p_{23}p_{32} - p_{34} \\ &= (p_{22u}p_{33u} - p_{23u}p_{32u})u_0^2 + (p_{22u}q_{33} - p_{32u}q_{23})u_0\tau(u_0)\varepsilon_r - q_{33}\tau(u_0)\varepsilon_\psi, \\ c_2 &= -p_{22} - p_{33} = -(p_{22u} + p_{33u})u_0 - q_{33}\tau(u_0)\varepsilon_r. \end{aligned}$$

The Routh-Hurwitz criterion, see [9], states that all eigenvalues of P have negative real part if and only if $c_2, c_0 > 0$ and $c_2c_1 - c_0 > 0$. The first condition is always satisfied for the HTC values and $\varepsilon_\psi > 0$ since $p_{22}, p_{33} < 0$, which implies $c_2 > 0$. In addition, $p_{24} > 0, p_{32}, p_{34}, p_{22} < 0$ yield $c_0 > 0$. Concerning the second condition, using K_{ij} from (3.4), a direct computation gives

$$c_2c_1 - c_0 = K_{11}\varepsilon_\psi\varepsilon_r + K_{02}\varepsilon_r^2 + K_{01}\varepsilon_r + K_{10}\varepsilon_\psi + K_{00}.$$

Since $\partial_{\varepsilon_\psi}c_0 > 0$ for the HTC, precisely those $(\varepsilon_r, \varepsilon_\psi)$ ‘above’ the convex curve defined by $c_2c_1 - c_0 = 0$, or equivalently (3.5), provide eigenvalues with negative real part. In addition, for the control values satisfying (3.5) and $\varepsilon_\psi(\varepsilon_r) \neq 0$, it follows that there exists a pair of complex conjugates with vanishing real part. Indeed, for $c_2c_1 - c_0 = 0$ the characteristic polynomial can be factorized as $Q_P(\lambda) = (c_2\lambda^2 + c_0)\left(\frac{1}{c_2}\lambda + 1\right)$, and since $c_2, c_0 > 0$, the eigenvalues of the first factor correspond to a pair of purely complex conjugates, $\lambda_\pm = \pm\sqrt{-c_1}$.

Finally, at $\varepsilon_\psi = 0$ the last column of the matrix (3.3) vanishes, which gives the fixed zero eigenvalue (and $c_0 = 0$). The conditions for the other eigenvalues to have negative real parts are $c_2, c_1 > 0$. Here $c_2 > 0$ holds as above since $p_{22}, p_{33} < 0$ for the HTC values and $\varepsilon_r \geq 0$. On the one hand, c_1 is linear in ε_r with positive slope and $c_1 < 0$ at $\varepsilon_r = 0$ for the HTC. Hence, c_1 changes sign from negative to positive at a unique $\varepsilon_{r_1} > 0$, and at ε_{r_1} the characteristic polynomial reads $Q_P(\lambda) = \lambda^2(\lambda + c_2)$, with a double root. On the other hand, since $c_0 = 0$ and $c_2 > 0$, the sign of c_1 is that of $c_2c_1 - c_0$ so that $\varepsilon_\psi(\varepsilon_r) = 0$ is the stability threshold as claimed. \square

Next we discuss the impact of varying the parameters D_p and x_T on the stabilization and thus linear controllability of the straight motion.

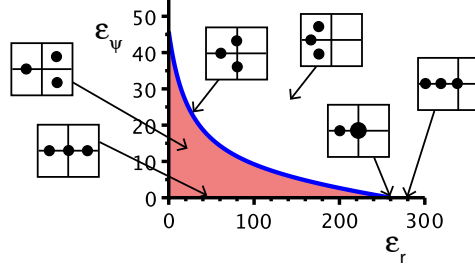


Figure 2: Stability boundary of the straight motion for the HTC values in the positive quadrant of the $(\varepsilon_r, \varepsilon_\psi)$ -plane. The insets illustrate the arrangement of the eigenvalues (in the complex-plane) on the boundary, the ε_r -axis and nearby. The straight motion is unstable in the colored area below the curve, and it is stable in the white region. The transition to stability for $\varepsilon_\psi > 0$ goes via a complex conjugate pair of eigenvalues, and the transition for $\varepsilon_\psi = 0$ by a real eigenvalue.

3.2.1 Impact of changing the parameter D_p

We scale the propeller diameter D_p as in §3.1: $u = D_p \tilde{u}$ and $\tau(u) = D_p^4 \tilde{\tau}(\tilde{u})$, so $\tilde{\tau}$ is independent of D_p and (3.5) becomes

$$\varepsilon_\psi(\varepsilon_r, \tilde{u}; D_p) = -\frac{\tilde{K}_{02} D_p^6 \tilde{u} \tilde{\tau}^2 \varepsilon_r^2 + \tilde{K}_{01} D_p^3 \tilde{u}^2 \tilde{\tau} \varepsilon_r + \tilde{K}_{00} \tilde{u}^3}{\tilde{K}_{11} D_p^5 \tilde{\tau}^2 \varepsilon_r + \tilde{K}_{10} D_p^2 \tilde{u} \tilde{\tau}}, \quad (3.7)$$

where \tilde{K}_{ij} are real constants. From (3.2) we have $\tilde{u}_0 = \tilde{u}_0(D_p) \rightarrow \tilde{u}_0^* \neq 0$, as $D_p \rightarrow \infty$. Setting $E := \tilde{\tau} D_p^3 \varepsilon_r$, $\Upsilon := \tilde{\tau} D_p^2$ in (3.7) gives an expression which has the same functional form with same signs of coefficients as (3.5). Thus, the stability boundary is qualitatively the same for different D_p . Specifically, on the one hand, for $\varepsilon_r = 0$ we get from (3.7) that $\varepsilon_\psi(0, \tilde{u}; D_p) = -\frac{\tilde{K}_{00} \tilde{u}^2}{\tilde{K}_{10} D_p^2 \tilde{\tau}} = \mathcal{O}(D_p^{-2})$. On the other hand, for $\varepsilon_\psi = 0$ in (3.7) we obtain the function $\varepsilon_r(\tilde{u}; D_p) = \frac{\tilde{u}}{D_p^3 \tilde{\tau}} \frac{-\tilde{K}_{01} \pm \sqrt{\tilde{K}_{01}^2 - 4\tilde{K}_{02} \tilde{K}_{00}}}{2\tilde{K}_{02}}$, and $\tilde{u}_0(D_p) \rightarrow \tilde{u}_0^* \neq 0$ implies $\varepsilon_r(\tilde{u}_0; D_p) = \mathcal{O}(D_p^{-3})$. We conclude that increasing the propeller diameter D_p enlarges the convex stable region in parameter space with different rates along the different axes. In fact, numerically this holds for all D_p .

3.2.2 Impact of changing the thruster position parameter x_T

As shown next, understanding the impact of x_T is more involved. For instance, taking $x_T > 0.18$, the P-control cannot stabilize the straight motion at all, thus creating an ‘uncontrollable’ situation.

Before preparing the precise statement and proof, we first note that while (3.1) does not depend on x_T , the function $\varepsilon_\psi(\varepsilon_r)$ in (3.5) does, and we therefore denote this as $\varepsilon_\psi(\varepsilon_r; x_T)$. However, it is not clear that the graph of $\varepsilon_\psi(\varepsilon_r; x_T)$ remains a stability boundary since this only accounts for one of the criteria for stable eigenvalues. The Routh-Hurwitz criterion in the proof of Theorem 3.1 also requires $c_2 > 0$, but, for instance at $x_T = 0.3$, we have $c_2 < 0$ for $\varepsilon_r > \varepsilon_{r_2} \approx 144.47$; see Fig. 3 (a). In this case the curve $\varepsilon_\psi(\varepsilon_r; x_T)$ is not a stability boundary, and the straight motion cannot be stabilized by the P-control (2.4). In the following we provide

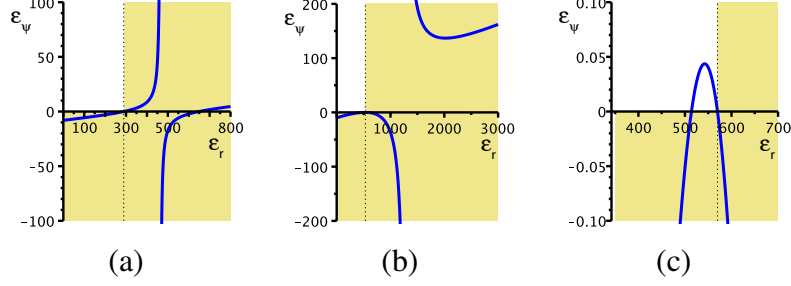


Figure 3: We display different forms of the curve $\varepsilon_\psi(\varepsilon_r; x_T)$ (blue) together with violations of the stability criteria $c_0 < 0, c_2 < 0$ (colored regions), where $c_0 < 0$ for $\varepsilon_\psi < 0$, and $c_2 < 0$ for large ε_r . (a) $x_T = 0.3$, (b) $x_T = x_{T_s} \approx 0.17$, and (c) $x_T = 0.16$, where we omit the second branch which is similar to that in (b).

a detailed (and somewhat tedious) analysis that explains all possibilities to stabilize the straight motion for different x_T under sign conditions that hold for the HTC.

The coefficients c_0, c_1, c_2 of the eigenvalue problem (3.6) can be written as

$$\begin{aligned} c_0 &= (k_{10} - k_{11}x_T)\varepsilon_\psi, \\ c_1 &= -k_{01} + (k_{10} - k_{11}x_T)\varepsilon_r + (k_{20} - k_{21}x_T)\varepsilon_\psi, \\ c_2 &= k_{02} + (k_{20} - k_{21}x_T)\varepsilon_r, \end{aligned} \quad (3.8)$$

where

$$\begin{aligned} k_{20} &:= D^{-1}m_{rv}\tau(u_0) > 0, & k_{21} &:= D^{-1}(m + m_{vv})\tau(u_0) > 0, \\ k_{10} &:= -D^{-1}N_\beta u_0\tau(u_0) > 0, & k_{11} &:= D^{-1}Y_\beta u_0\tau(u_0) > 0, \\ k_{02} &:= D^{-1} [m_{vr}N_\beta - (I_z + m_{rr})Y_\beta - (m + m_{vv})N_\gamma + m_{rv}(Y_\gamma - m)] u_0 > 0, \\ k_{01} &:= D^{-1}(mN_\beta + N_\gamma Y_\beta - N_\beta Y_\gamma)u_0^2 > 0. \end{aligned} \quad (3.9)$$

With these definitions, the function (3.5) reads

$$\varepsilon_\psi(\varepsilon_r; x_T) = \frac{\left(k_{02}(k_{10} - k_{11}x_T) + (k_{20} - k_{21}x_T)(k_{01} + (k_{10} - k_{11}x_T)\varepsilon_r) \right) \varepsilon_r - k_{02}k_{01}}{k_{10} - k_{11}x_T + (k_{20} - k_{21}x_T)(k_{02} + (k_{20} - k_{21}x_T)\varepsilon_r)}. \quad (3.10)$$

The denominator has a unique root with respect to ε_r given by

$$\varepsilon_r^* = \frac{k_{10} - k_{02}k_{20} - (k_{11} - k_{02}k_{21})x_T}{(k_{20} - k_{21}x_T)^2}, \quad (3.11)$$

i.e., $\varepsilon_\psi(\cdot; x_T)$ possesses a singularity at $\varepsilon_r = \varepsilon_r^*$; see Fig. 5 (a). For the HTC, large negative values of x_T yield negative $\varepsilon_r^* < 0$, a sign change occurs at $x_T \approx -0.38$, and there is a singularity near $x_T = 0.016$; see Fig. 4. In particular, $\varepsilon_r^* < 0$ for the HTC default value $x_T \approx -0.49$. As long as $\varepsilon_r^* < 0$, the singularity lies outside the positive range of the control parameters and is thus disregarded. However, for values of x_T where $\varepsilon_r^* > 0$, stabilization by ε_ψ alone is not possible. We plot an example in Fig. 5 (a). For $\varepsilon_r^* > 0$, there can be two positive values of ε_r for which

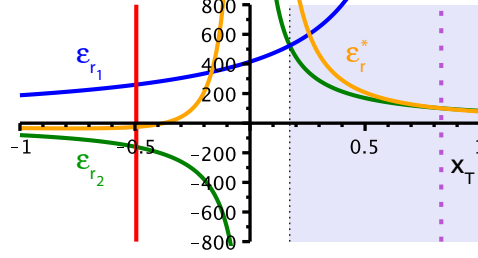


Figure 4: We plot relevant quantities for the HTC as functions of x_T . We mark the default HTC value $x_T = -0.49429$ (red vertical line), the region $x_T > x_{T_s} \approx 0.17$ (shaded area) and $x_T = x_{T_1} \approx 0.83$ (purple pointed line). Orange curves: $\varepsilon_r^*(x_T)$ from (3.11) for the singularity of $\varepsilon_\psi(\varepsilon_r; x_T)$; blue curve: $\varepsilon_{r_1}(x_T)$, the root of c_1 at $\varepsilon_\psi = 0$; green curves: $\varepsilon_{r_2}(x_T)$, the root of c_2 . The domain $[-0.5, 0.5]$ of x_T is extended to illustrate better the shape of the curves and the location of x_{T_1} .

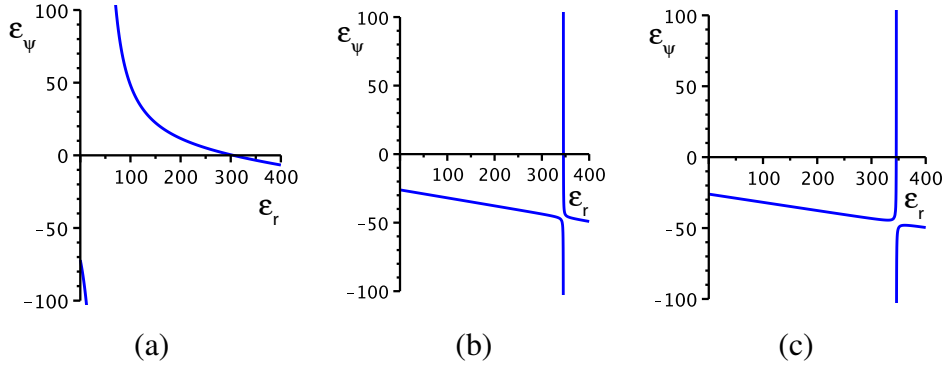


Figure 5: The function $\varepsilon_\psi(\varepsilon_r; x_T)$ is plotted for the HTC and (a) $x_T = -0.3$, where $\varepsilon_r^* \approx 41.88$; (b) $x_T = -0.1669$; and (c) $x_T = -0.1668$.

$\varepsilon_\psi(\varepsilon_r; x_T) = 0$, i.e., potentially a stabilization and subsequent destabilization when increasing ε_r from zero. We plot examples in Fig. 3 (a) and (c). In addition, comparing Figs. 5 (a) and 3 (a), a switching from convexity to concavity of $\varepsilon_\psi(\varepsilon_r; x_T)$ has occurred. For the HTC this lies at $x_T \approx -0.17$; cf. Fig. 5 (b,c). At this switching point (3.10) degenerates. This will be treated as a special case further below.

Otherwise, whenever stabilization of the straight motion is possible, the stability region is bounded by the graph of $\varepsilon_\psi(\varepsilon_r; x_T)$ from (3.10), which gives the solutions to $c_2 c_1 = c_0$. Its intersections with the ε_r -axis, if defined, are

$$\varepsilon_{r_1} := \frac{k_{01}}{k_{10} - k_{11}x_T}, \quad \varepsilon_{r_2} := -\frac{k_{02}}{k_{20} - k_{21}x_T}.$$

At these values and $\varepsilon_\psi = 0$ we have $c_1 = 0$ and $c_2 = 0$, respectively. For the HTC, ε_{r_1} already appeared in the proof of Theorem 3.1. If both are defined, so is ε_r^* , and we can write

$$\varepsilon_\psi(\varepsilon_r; x_T) = a \frac{(\varepsilon_r - \varepsilon_{r_1})(\varepsilon_r - \varepsilon_{r_2})}{\varepsilon_r - \varepsilon_r^*}, \quad a := -\frac{k_{10} - k_{11}x_T}{k_{20} - k_{21}x_T}. \quad (3.12)$$

For a given ordering of $\varepsilon_{r_1}, \varepsilon_{r_2}, \varepsilon_r^*$ and sign of a , we can read off the shape of the stability boundary as a function of ε_r . The ordering depends on x_T , and relevant thresholds will be

$$x_{T_1} := \frac{k_{10}}{k_{11}} = \frac{N_\beta}{Y_\beta}, \quad x_{T_2} := \frac{k_{20}}{k_{21}} = \frac{m_{rv}}{m + m_{vv}}, \quad x_{T_3} := \frac{k_{01}k_{20} + k_{02}k_{10}}{k_{01}k_{21} + k_{02}k_{11}}, \quad (3.13)$$

corresponding to the value of x_T where ε_{r_1} is undefined (and $c_0 = 0$), ε_{r_2} is undefined, or $\varepsilon_{r_1} = \varepsilon_{r_2}$, respectively. Here $x_{T_3} > 0$ under the sign conditions (3.9). These special values of x_T are independent of u_0 and thus of D_p . For the HTC the quantities in (3.13) have the values noted in Fig. 6 and $x_{T_1} \approx 0.83$. In this figure we also plot the values x_{T_0}, x_{T_-} . The first solves $\varepsilon_r^* = 0$ and has the explicit expression $x_{T_0} = (k_{02}k_{20} - k_{10}) / (k_{02}k_{21} - k_{11})$. The threshold x_{T_-} is the smallest solution to $\varepsilon_r^* = \varepsilon_{r_1}$ for the HTC. This equation is generally quadratic with respect to x_T , but it is not clear that the roots are real under the conditions (3.9). If these are real, then the smaller solution means a transition from convex to concave stability boundary for $\varepsilon_\psi, \varepsilon_r > 0$.

Regarding signs and monotonicity we note that (3.9) implies, if x_T is none of (3.13),

$$\begin{aligned} \operatorname{sgn}(\varepsilon_{r_1}) &= \operatorname{sgn}(x_{T_1} - x_T), & \operatorname{sgn}(a) &= \operatorname{sgn}((x_{T_1} - x_T)(x_T - x_{T_2})), \\ \operatorname{sgn}(\varepsilon_{r_2}) &= \operatorname{sgn}(x_T - x_{T_2}), & \partial_{x_T} \varepsilon_{r_1} &> 0, \quad \partial_{x_T} \varepsilon_{r_2} < 0, \end{aligned} \quad (3.14)$$

cf. Fig. 4. In the case $\varepsilon_{r_1} = \varepsilon_r^*$ and $x_T \neq x_{T_2}$, the singularity of (3.12) degenerates into a vertical graph that may form the stability boundary. Indeed, $c_1 c_2 = c_0$ can then be written as

$$(\varepsilon_r - \varepsilon_{r_1})(\varepsilon_\psi - a(\varepsilon_r - \varepsilon_{r_2})) = 0, \quad \varepsilon_{r_1} = \varepsilon_r^*. \quad (3.15)$$

With these preparations we present our main linear stability result. As before, the stability region and its boundary refer to the positive quadrant in the $(\varepsilon_r, \varepsilon_\psi)$ -plane.

Theorem 3.2. *Consider x_T as a free parameter and assume for all other parameters the signs of coefficients within c_0, c_1, c_2 as in (3.9) as well as $X_{|u|} < 0$, $\tau(0) > 0$. Then two scenarios occur. In case $x_{T_2} < x_{T_1}$, for any $x_T \leq x_{T_2}$ the statement of Theorem 3.1 holds true for all $\underline{\varepsilon}_r > 0$. Furthermore, the stability boundary (3.5) is a vertical line or a strictly monotone function of ε_r , intersecting the ε_r -axis, but possibly not the ε_ψ -axis with a vertical asymptote at $\varepsilon_r = \varepsilon_r^*$. Moreover, if $x_T \geq x_{T_3}$, the straight motion cannot be stabilized by any $\varepsilon_r, \varepsilon_\psi > 0$, while for $x_{T_2} < x_T < x_{T_3}$, the stability region is bounded with boundary of parabolic shape, intersecting twice the ε_r -axis. In case $x_{T_1} \leq x_{T_2}$, the stability boundary is strictly monotone or vertical if $x_T < x_{T_1}$ and otherwise stabilization is impossible.*

In all cases which admit stabilization, the real part of the critical eigenvalue(s) has non-zero derivative as $(\varepsilon_r, \varepsilon_\psi) \geq 0$ transversally crosses the stability boundary along a curve.

In the final statement, transversal crossing means that the curve's tangent vector at the crossing point is linearly independent of the stability boundary's tangent vector.

Before presenting the proof we proceed with some remarks. The theorem in particular implies the following alternative: either the straight motion can be stabilized by increasing ε_r for all $\varepsilon_\psi \geq 0$ or none, except in the case of a bounded stability region; cf. Fig. 6. In all cases, the possibility to stabilize is determined by the case $\varepsilon_\psi = 0$ alone. The theorem implies that, given

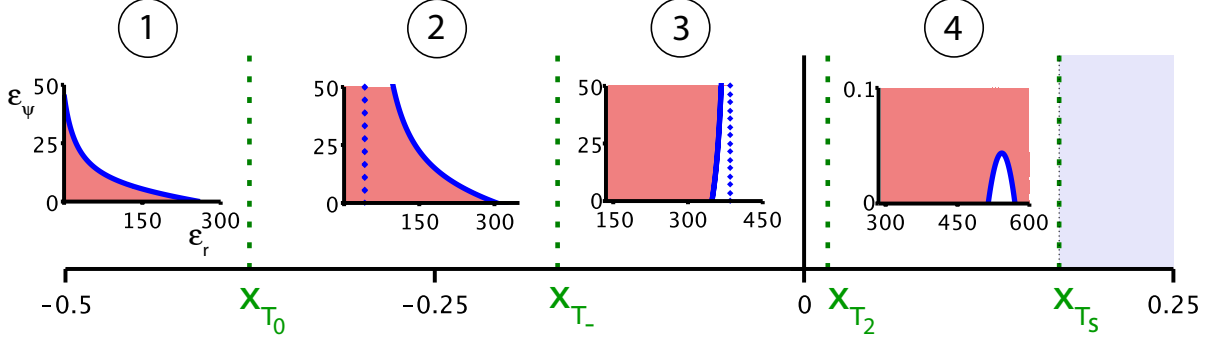


Figure 6: HTC parameters with varying x_T . Each inset shows the shape of the stability region in the $(\varepsilon_r, \varepsilon_\psi)$ -plane for x_T in the corresponding interval on the x_T -axis. Unstable region is shaded red, blue line the stability boundary, vertical dashed line its vertical asymptote, if present. For $x_T > x_{T_s}$ stabilization is not possible. Case 1: $x_T \in [-0.5, x_{T_0})$, $x_{T_0} \approx -0.38$, inset for $x_T \approx -0.49$. Case 2: $x_T \in (x_{T_0}, x_{T_-})$, $x_{T_-} \approx -0.17$, inset for $x_T = -0.3$. Case 3: $x_T \in (x_{T_-}, x_{T_2})$, $x_{T_2} \approx 0.016$, inset for $x_T \approx -0.16$. Case 4: $x_T \in (x_{T_2}, x_{T_s})$, $x_{T_s} \approx 0.17$, inset for $x_T \approx 0.16$.

the signs in (3.9), any sufficiently large x_T makes it impossible to stabilize the straight motion by the P-control (2.4). But a necessary condition for this lack of controllability to be physically meaningful is $x_{T_s} < 1/2$ or $x_{T_1} < 1/2$. Specifically, for the HTC values, we have $x_{T_2} < x_{T_s} < x_{T_1}$ with $x_{T_s} \approx 0.17$; cf. Fig. 6. The decisive thresholds x_{T_1} and x_{T_2} have the surprisingly simple expressions $m_{rv}/(m + m_{vv})$ and N_β/Y_β , respectively, which depend purely on non-dimensional mass and hydrodynamic coefficients of the hull.

Proof of Theorem 3.2. If $X_{u|u|} < 0$ and $\tau(0) > 0$, then $u_0, \tau(u_0) > 0$ by (3.1), which has a unique positive solution. The Routh-Hurwitz criterion from the proof of Theorem 3.1 consists of $c_0, c_2 > 0$ and $c_2 c_1 > c_0$; cf. (3.8). These conditions must be attainable with $\varepsilon_r \geq 0, \varepsilon_\psi > 0$ in order to stabilize the straight motion, while for $\varepsilon_\psi = 0$ we have $c_0 = 0$ and the criterion becomes $c_1, c_2 > 0$. The common condition $c_2 > 0$ is independent of ε_ψ and equivalent to either $x_T \leq x_{T_2}$ (and any $\varepsilon_r \geq 0$), or $\varepsilon_r < \varepsilon_{r_2}$; see Figure 3.

Concerning $\varepsilon_\psi = 0$, since $k_{10}, k_{01}, k_{11} > 0$, we have $c_1 > 0$ if and only if $x_T < x_{T_1}$ and $\varepsilon_r > \varepsilon_{r_1}$, but only $\varepsilon_{r_1} \geq 0$ is a relevant constraint. In case $x_T > x_{T_2}$, both $c_2 > 0$ and $c_1 > 0$ can be satisfied if and only if $\varepsilon_{r_1} < \varepsilon_{r_2}$, which is equivalent to $x_T < x_{T_s}$. Hence, controllability for $\varepsilon_\psi = 0$ requires $x_T < \min\{x_{T_1}, \max\{x_{T_2}, x_{T_s}\}\}$, which covers the claimed statements in this case.

We now turn to controllability for $\varepsilon_\psi > 0$. The condition $c_0 > 0$ is then equivalent to $x_T < x_{T_1}$ as claimed for a possible stabilization. We may therefore assume $x_T < x_{T_1}$ in the following reasoning, which implies $\varepsilon_{r_1} > 0$ by (3.14). It remains to incorporate the last condition, $c_1 c_2 > c_0$, whose boundary is defined by $\varepsilon_\psi(\varepsilon_r; x_T)$ from (3.10). Since $\partial_{\varepsilon_\psi}(c_1 c_2 - c_0) = 0$ precisely at singularities of its graph, the stable region lies above or below this boundary unless it is vertical; cf. (3.15). We treat this case separately at the end and thus assume for now that $\varepsilon_{r_1} \neq \varepsilon_r^*$.

In case $x_T = x_{T_2} < x_{T_1}$, i.e., $k_{20} = k_{21} x_T$, we have $\varepsilon_\psi(\varepsilon_r; x_T) = k_{02}(\varepsilon_r - k_{01}/(k_{10} - k_{11} x_T))$ with positive slope and root at ε_{r_1} with respect to ε_r . This corresponds to the stability boundary for $\varepsilon_\psi > 0$ since $c_2, c_0 > 0$ due to the assumption $x_T = x_{T_2} < x_{T_1}$ and $k_{02} > 0$. In this case $\partial_{\varepsilon_\psi}(c_1 c_2 - c_0) = -(k_{20} - k_{21} x_T) < 0$. Therefore, the stable region is below this boundary.

The case $x_T \neq x_{T_2}$ is more involved and we use (3.12). Since $x_T < x_{T_1}$, both ε_{r_1} and ε_{r_2} exist, and either $\varepsilon_{r_1} < \varepsilon_r^* < \varepsilon_{r_2}$ or $\varepsilon_r^* > \max\{\varepsilon_{r_1}, \varepsilon_{r_2}\}$ due to

$$\varepsilon_r^* = \varepsilon_{r_2} + (k_{10} - k_{11}x_T)/(k_{20} - k_{21}x_T)^2 > \varepsilon_{r_2}. \quad (3.16)$$

A direct computation gives $\partial_{\varepsilon_r} \varepsilon_{\psi}(\varepsilon_r; x_T) = 0$ at $\varepsilon_r = \varepsilon_r^* \pm \sqrt{(\varepsilon_r^* - \varepsilon_{r_1})(\varepsilon_r^* - \varepsilon_{r_2})}$ so that the graph of $\varepsilon_{\psi}(\cdot; x_T)$ has at most one critical point on either side of the singularity $\varepsilon_r = \varepsilon_r^*$. Thus, in case $\varepsilon_{r_1} < \varepsilon_r^* < \varepsilon_{r_2}$ the branches of the graph are monotone on $(\varepsilon_{r_1}, \varepsilon_r^*)$ and $(\varepsilon_r^*, \varepsilon_{r_2})$, respectively. In case $\varepsilon_r^* > \max\{\varepsilon_{r_1}, \varepsilon_{r_2}\}$ the branches are monotone on $(\max\{\varepsilon_{r_1}, \varepsilon_{r_2}\}, \varepsilon_r^*)$ and $(\varepsilon_r^*, \infty)$, respectively. The type of monotonicity and the sign of $\varepsilon_{\psi}(\cdot; x_T)$ can be inferred from the slopes at $\varepsilon_{r_1}, \varepsilon_{r_2}$, when given their ordering with respect to ε_r^* . On the one hand, by a direct computation we have

$$\partial_{\varepsilon_r} \varepsilon_{\psi}(\varepsilon_{r_1}; x_T) = a \frac{(\varepsilon_{r_1} - \varepsilon_{r_2})(\varepsilon_{r_1} - \varepsilon_r^*)}{(\varepsilon_{r_1} - \varepsilon_r^*)^2}, \quad (3.17)$$

which has the sign of $(x_T - x_{T_2})(\varepsilon_{r_1} - \varepsilon_{r_2})(\varepsilon_{r_1} - \varepsilon_r^*)$ due to (3.14) and the assumption $x_T < x_{T_1}$. On the other hand, we compute $\partial_{\varepsilon_r} \varepsilon_{\psi}(\varepsilon_{r_2}; x_T) = (k_{20} - k_{21}x_T)(\varepsilon_{r_2} - \varepsilon_{r_1})$. Together with the previous we conclude

$$\begin{aligned} \operatorname{sgn}(\partial_{\varepsilon_r} \varepsilon_{\psi}(\varepsilon_{r_1}; x_T)) &= \operatorname{sgn}((x_T - x_{T_2})(\varepsilon_{r_1} - \varepsilon_{r_2})(\varepsilon_{r_1} - \varepsilon_r^*)), \\ \operatorname{sgn}(\partial_{\varepsilon_r} \varepsilon_{\psi}(\varepsilon_{r_2}; x_T)) &= \operatorname{sgn}((x_{T_2} - x_T)(\varepsilon_{r_2} - \varepsilon_{r_1})). \end{aligned} \quad (3.18)$$

With these preparations, we discuss the claimed geometry of stability boundary for $\varepsilon_{\psi} > 0$ and the different cases.

(I). The case $x_T < x_{T_1}$ and $x_T \leq x_{T_2}$. This applies to both situations of the theorem statement and we have already inferred $c_2, c_0 > 0$. Suppose $x_T < x_{T_2}$. From (3.14) it follows that $\varepsilon_{r_2} < 0 < \varepsilon_{r_1}$, which means that ε_{r_1} lies at the unique intersection point of the graph of $\varepsilon_{\psi}(\cdot; x_T)$ with the ε_r -axis. Hence, to prove the claim that Theorem 3.1 holds true for all $\underline{\varepsilon}_r > 0$, it suffices to show that the graph also intersects the positive ε_{ψ} -axis or is positive with vertical asymptote. As argued above, this is ensured if $\partial_{\varepsilon_r} \varepsilon_{\psi}(\varepsilon_{r_1}; x_T) < 0$. Since $\varepsilon_{r_1} > \varepsilon_{r_2}$ in the present situation, this sign is indeed negative for $\varepsilon_r^* < \varepsilon_{r_1}$ due to (3.18). In the case $\varepsilon_r^* > \varepsilon_{r_1}$ the sign is positive, but the graph is positive for $\varepsilon_{r_1} < \varepsilon_r < \varepsilon_r^*$ with a vertical asymptote at ε_r^* ; compare Fig. 5. For $x_T = x_{T_2}$ we already found above that the graph is linear with positive slope and root at $\varepsilon_r = \varepsilon_{r_1} > 0$.

(II). The case $x_{T_2} < x_{T_1}$. We first note that the subcase $x_T \geq x_{T_3}$ in the theorem statement certainly occurs since $x_{T_3} > x_{T_2}$ follows from $x_{T_2} < x_{T_1}$ by direct calculation and using (3.9). Suppose $x_T > x_{T_3}$. Then, $\varepsilon_{r_1} > \varepsilon_{r_2} > 0$ holds due to (3.14) and $\varepsilon_{r_1} = \varepsilon_{r_2}$ at $x_T = x_{T_3}$. Therefore, (3.18) implies $\partial_{\varepsilon_r} \varepsilon_{\psi}(\varepsilon_{r_2}) > 0$. Due to the sign of the slope and $\varepsilon_r^* > \varepsilon_{r_2}$, the function $\varepsilon_{\psi}(\cdot; x_T)$ takes negative values for $\varepsilon_r < \varepsilon_{r_2}$. However, $x_T > x_{T_2}$ implies $c_2 < 0$ for $\varepsilon_r > \varepsilon_{r_2}$, which means stabilization is possible for $\varepsilon_r < \varepsilon_{r_2}$ only. Thus, as claimed, stabilization of the straight motion by $\varepsilon_{\psi} > 0$ is not possible for $x_T > x_{T_3}$.

Suppose now $x_T = x_{T_3}$. Here $\varepsilon_{r_1} = \varepsilon_{r_2} < \varepsilon_r^*$ so that $\partial_{\varepsilon_r} \varepsilon_{\psi}(\varepsilon_{r_1}) = 0$ and $a > 0$ due to (3.14). In the relevant range $\varepsilon_r < \varepsilon_{r_2}$, the function $\varepsilon_{\psi}(\cdot; x_T)$ again takes negative values and hence, stabilization is not possible; see Fig. 3 (b).

Since $x_T = x_{T_2}$ was discussed in (I) above, the last subcase is $x_{T_2} < x_T < x_{T_3}$. Analogous to before, the signs and monotonicity relations (3.14) and (3.16) imply $0 < \varepsilon_{r_1} < \varepsilon_{r_2} < \varepsilon_r^*$. It

follows that $\varepsilon_\psi(\cdot; x_T)$ is smooth for $\varepsilon_r \leq \varepsilon_{r_2}$, positive for $\varepsilon_{r_1} < \varepsilon_r < \varepsilon_{r_2}$ and negative for $\varepsilon_r < \varepsilon_{r_1}$. Its parabolic shape follows from the quadratic numerator of $\varepsilon_\psi(\cdot; x_T)$.

(III). The case $x_{T_1} \leq x_{T_2}$. As shown above, stabilization is possible if $x_T < x_{T_1}$, but is impossible for $x_T > x_{T_1}$. The marginal case $x_T = x_{T_1}$ implies $c_0 = 0$, i.e., a zero eigenvalue, and at $\varepsilon_\psi = 0$ we obtain $c_1 = -k_{01} < 0$, which implies instability. Therefore, stabilization in the sense of the theorem statement is not possible.

We come to the degenerate situation (3.15), which needs $x_T \neq x_{T_2}$. Since (3.14) and (3.16) hold, $\varepsilon_{r_1} = \varepsilon_r^*$ requires $x_T < x_{T_1}$ and $x_T < x_{T_2}$ so that $a < 0$ and $\varepsilon_{r_2} \leq 0 < \varepsilon_{r_1}$. Then the linear branch of (3.15) has negative slope a and is non-positive at $\varepsilon_r = 0$. Hence, it lies outside the relevant range and the vertical branch is the stability boundary.

It remains to prove non-zero derivatives of the real part of the critical eigenvalue(s) with respect to the control parameters $\varepsilon_\psi = \varepsilon_\psi^0, \varepsilon_r = \varepsilon_r^0$ on the stability boundary. In the case $\varepsilon_\psi^0 = 0$, a transverse crossing goes along the ε_r -axis. Here (3.6) reduces to $\lambda^2 + c_2\lambda + c_1 = 0$ so that $\partial_{\varepsilon_r}\lambda = -\frac{\partial_{\varepsilon_r}c_1}{c_2} = -\frac{k_{10}-k_{11}x_T}{c_2}$, which is negative since $x_T < x_{T_1}$.

In the case $\varepsilon_\psi^0 > 0$, the critical eigenvalues $\pm i\sqrt{c_1}$ have common real part μ for nearby $\varepsilon_r, \varepsilon_\psi$. Upon implicitly differentiating (3.6), a direct computation for $\varepsilon \in \{\varepsilon_r, \varepsilon_\psi\}$ yields

$$\partial_\varepsilon \mu(\varepsilon_r^0, \varepsilon_\psi^0) = -\frac{\partial_\varepsilon(c_1c_2 - c_0)}{2(c_1 + c_2^2)}(\varepsilon_r^0, \varepsilon_\psi^0), \quad (3.19)$$

which is well-defined since $c_1, c_2 > 0$ on the stability boundary. In the case (3.15), $\varepsilon = \varepsilon_r$ for a transverse crossing and (3.15) gives $\partial_\varepsilon(c_1c_2 - c_0) = \varepsilon_\psi - a(\varepsilon_r - \varepsilon_{r_2})$. This is positive since we found above $a < 0$, and in this case, $\varepsilon_{r_1} > \varepsilon_{r_2}$ holds. Otherwise, the boundary is in a smooth branch of $\varepsilon_\psi(\varepsilon_r; x_T)$ and from its definition we have

$$\varepsilon'_\psi(\varepsilon_r^0; x_T) = -\partial_{\varepsilon_r}(c_1c_2 - c_0)/b, \quad b := \partial_{\varepsilon_\psi}(c_1c_2 - c_0)(\varepsilon_r^0, \varepsilon_\psi^0).$$

Due to the fact that $b \neq 0$, (3.19) is non-zero for $\varepsilon = \varepsilon_\psi$. For $\varepsilon = \varepsilon_r$, the numerator can be written as $-b\varepsilon'_\psi(\varepsilon_r^0; x_T)$, which vanishes on the stability boundary precisely at the local maximum when this is parabolic, i.e., for $x_{T_2} < x_T < x_{T_1}$. \square

The study of linear stability is completed and now we move to the nonlinear analysis.

3.3 Bifurcation Analysis

In this section we analyze the nonlinear effects of the stabilizing control based on the linear stability analysis of the previous section. In order facilitate the bifurcation analysis, we first shift the straight motion equilibrium point $(u_0, 0, 0, 0)$ of (2.7) to the origin by writing the surge variable as $u = u_0 + \tilde{u}$. In terms of (\tilde{u}, v, r, ψ) we thus obtain

$$\begin{pmatrix} \dot{\tilde{u}} \\ \dot{v} \\ \dot{r} \\ \dot{\psi} \end{pmatrix} = M^{-1} \begin{pmatrix} mvr + X_H(\tilde{u}) + \tau(u_0 + \tilde{u}) \cos \eta \\ -m(u_0 + \tilde{u})r + Y_H(\tilde{u}) + \tau(u_0 + \tilde{u}) \sin \eta \\ N_H(\tilde{u}) + x_T \tau(u_0 + \tilde{u}) \sin \eta \\ r \end{pmatrix}. \quad (3.20)$$

In the following we omit the tilde from \tilde{u} to simplify the notation. We rewrite, expand in u and, based on the results in [18], already omit all cubic-order terms, which yield

$$\begin{pmatrix} \dot{u} \\ \dot{v} \\ \dot{r} \\ \dot{\psi} \end{pmatrix} = \begin{pmatrix} \tau_{11}(\cos \eta - 1) + z_1 u + z_2 u^2 + z_3 v r + [\tau_{12} u + \tau_{13} u^2] \cos \eta \\ p_{22} v + z_5 r + z_6 u v + z_7 u r + f_1(v, r) + [\tau_{21} + \tau_{22} u + \tau_{23} u^2] \sin \eta \\ p_{32} v + z_9 r + z_{10} u v + z_{11} u r + f_2(v, r) + [\tau_{31} + \tau_{32} u + \tau_{33} u^2] \sin \eta \\ r \end{pmatrix}. \quad (3.21)$$

The coefficients z_j, τ_{ij} result directly from the expansion, but their explicit forms are not used in the following abstract analysis. The functions f_1, f_2 read

$$f_1(v, r) = a_{11} v |v| + a_{12} v |r| + a_{21} r |v| + a_{22} r |r|, \quad f_2(v, r) = b_{11} v |v| + b_{12} v |r| + b_{21} r |v| + b_{22} r |r|,$$

with coefficients

$$\begin{aligned} a_{11} &= D^{-1} \left((I_z + m_{rr}) Y_{\beta|\beta} - m_{vr} N_{\beta|\beta} \right), & a_{12} &= D^{-1} (I_z + m_{rr}) Y_{\beta|\gamma}, \\ a_{21} &= D^{-1} (I_z + m_{rr}) Y_{\beta|\gamma}, & a_{22} &= D^{-1} \left((I_z + m_{rr}) Y_{\gamma|\gamma} - m_{vr} N_{\gamma|\gamma} \right), \\ b_{11} &= D^{-1} \left((m + m_{vv}) N_{\beta|\beta} - m_{rv} Y_{\beta|\beta} \right), & b_{12} &= -D^{-1} m_{rv} Y_{\beta|\gamma}, \\ b_{21} &= -D^{-1} m_{rv} Y_{\beta|\gamma}, & b_{22} &= D^{-1} \left((m + m_{vv}) N_{\gamma|\gamma} - m_{rv} Y_{\gamma|\gamma} \right). \end{aligned}$$

Using again that our analysis focuses on the vicinity of the origin, we expand the functions $\cos \eta = 1 + \mathcal{O}(\eta^2)$, $\sin \eta = \eta + \mathcal{O}(\eta^3)$ and omit higher-order terms. Using the control form $\eta = \varepsilon_r r + \varepsilon_\psi \psi$ from (2.4) this reduces (3.21) to

$$\begin{pmatrix} \dot{u} \\ \dot{v} \\ \dot{r} \\ \dot{\psi} \end{pmatrix} = \begin{pmatrix} p_{11} u + U(u, v, r) \\ p_{22} v + p_{23} r + p_{24} \psi + z_6 u v + (z_7 + \tau_{22} \varepsilon_r) u r + \tau_{22} \varepsilon_\psi u \psi + f_1(v, r) \\ p_{32} v + p_{33} r + p_{34} \psi + z_{10} u v + (z_{11} + \tau_{32} \varepsilon_r) u r + \tau_{32} \varepsilon_\psi u \psi + f_2(v, r) \\ r \end{pmatrix}, \quad (3.22)$$

where $U(u, v, r)$ is a second-order nonlinear function. In agreement with §3.2, the coefficients are $p_{11} = z_1 + \tau_{12}$, $p_{23} = z_5 + \tau_{21} \varepsilon_r$, $p_{24} = \tau_{21} \varepsilon_\psi$, $p_{33} = z_9 + \tau_{31} \varepsilon_r$, $p_{34} = \tau_{31} \varepsilon_\psi$, i.e., the entries of the matrix A from (3.3). In particular, the linear part A possesses a diagonal block structure with the eigenvalue $\lambda_1 = p_{11}$ and a lower right 3×3 -submatrix block.

As a first step towards the nonlinear analysis, we discuss the simpler case of the pitchfork bifurcation, and then turn to the more involved Hopf bifurcation analysis.

3.3.1 Pitchfork bifurcation for $\varepsilon_\psi = 0$

We keep $\varepsilon_\psi = 0$ fixed so that the last equation in (3.22) can be dropped. Hence, the linear part A reduces to its upper left 3×3 -submatrix that consists of a block $\lambda_1 = p_{11} < 0$ as well as the 2×2 -block $B = (p_{ij})_{2 \leq i, j \leq 3}$. Theorem 3.1 implies that B possesses an eigenvalue $\lambda < 0$ as well as an eigenvalue that crosses through zero as ε_r crosses through ε_{r_1} , which is a unique positive value for the HTC. In particular, $B_0 := B|_{\varepsilon_r = \varepsilon_{r_1}}$ has eigenvectors e_0 for the zero eigenvalue and e_1 for λ , and the bifurcation upon changing ε_r will be purely of steady states. We thus seek

solutions of the reduced (3.22) with zero left-hand side. Since f_1, f_2 are quadratic of second-order modulus type, we expect a nonsmooth pitchfork bifurcation as in the truncated normal form $\sigma x|x| + \tilde{\varepsilon}_r x = 0$. Here x is the unknown variable and the sign of the parameter $\sigma \neq 0$ determines the super- or subcritical character of the bifurcation.

The first steady state equation of the reduced (3.22) can be solved for u by the implicit function theorem since $\lambda_1 = p_{11} < 0$ and U is nonlinear. The resulting solution satisfies $u = \mathcal{O}(v^2 + r^2)$ so that substitution into the second and third equations contributes to a term of cubic-order. In order to unfold the bifurcation, we write $\varepsilon_r = \varepsilon_{r_1} + \tilde{\varepsilon}_r$ so that $B = B_0 + \tilde{\varepsilon}_r B_1$ with a matrix B_1 that has vanishing first column. Next we choose the eigenvectors e_j^* of the adjoint B_0^\top such that $\langle e_j, e_{1-j}^* \rangle = 0$ and $\langle e_j, e_j^* \rangle = 1$, $j = 1, 2$. Changing coordinates $(v, r) = xe_0 + ye_1$, we project the second and third equations onto $\text{span}(e_1)$, which results in

$$\begin{aligned} 0 &= \langle (B_0 + \tilde{\varepsilon}_r B_1)(xe_0 + ye_1), e_1^* \rangle + \langle f(v, r), e_1^* \rangle \\ &= \lambda y + \tilde{\varepsilon}_r (x \langle B_1 e_0, e_1^* \rangle + y \langle B_1 e_1, e_1^* \rangle) + \langle f(v, r), e_1^* \rangle. \end{aligned}$$

Again, we may solve by the implicit function theorem since $\lambda < 0$, which yields $y = y(\tilde{\varepsilon}_r, x) = \mathcal{O}(|\tilde{\varepsilon}_r x| + x^2)$. It remains to solve the projection onto $\text{span}(e_0)$, which is given by

$$\begin{aligned} 0 &= \langle (B_0 + \tilde{\varepsilon}_r B_1)(xe_0 + ye_1), e_0^* \rangle + \langle f(v, r), e_0^* \rangle \\ &= \tilde{\varepsilon}_r (x \langle B_1 e_0, e_0^* \rangle + y \langle \tilde{\varepsilon}_r, x \rangle \langle B_1 e_1, e_0^* \rangle) + \langle f(v, r), e_0^* \rangle \\ &= \tilde{\varepsilon}_r x \langle B_1 e_0, e_0^* \rangle + x|x| \langle f(e_0), e_0^* \rangle + \mathcal{O}(3), \end{aligned}$$

where $\mathcal{O}(3)$ is of cubic-order in $\tilde{\varepsilon}_r, x$, and where we used that f is of second-order modulus form. Thus, the truncated bifurcation equation reads

$$\tilde{\varepsilon}_r x \langle B_1 e_0, e_0^* \rangle + x|x| \langle f(e_0), e_0^* \rangle = 0. \quad (3.23)$$

This gives the normal form since $\langle B_1 e_0, e_0^* \rangle$ coincides with the derivative with respect to the eigenvalue that is non-zero by Theorem 3.2. Numerical evaluation for the default HTC values yields the negative coefficients

$$\langle B_1 e_0, e_0^* \rangle \approx -4.04 \cdot 10^{-2}, \quad \langle f(e_0), e_0^* \rangle \approx -1.32 \cdot 10^{-3}.$$

Therefore, a nonsmooth pitchfork bifurcation occurs and it is supercritical since the steady state is stable for $\tilde{\varepsilon}_r > 0$. This means that a branch of stable steady motions emerges when decreasing ε_r from ε_{r_1} . Indeed, we numerically find this as plotted in Fig. 7.

Within the 4D system (3.22), this pitchfork bifurcation manifests as follows. We recall from §3.1 that for any $\varepsilon_r \geq 0, \varepsilon_\psi > 0$, the straight motion $(u_0, 0, 0, 0)$ appears as the unique equilibrium point with positive $u = u_0$ solving (3.1). However, for $\varepsilon_\psi = 0$ a line of equilibria appears, given by $(u_0, 0, 0, \psi)$ with arbitrary ψ .

On the one hand, let $r_+ > 0 > r_-$ be the r -components of the bifurcating equilibria in the 3D system. Then, due to $\dot{\psi} = r$, the ψ -components of the corresponding solutions in the 4D system with initial $\psi(0) = \psi_\pm(0)$ are, respectively,

$$\psi_\pm(t) := r_\pm t + \psi_\pm(0). \quad (3.24)$$

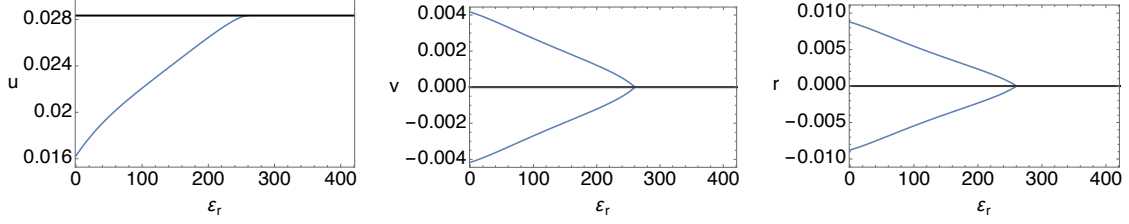


Figure 7: The nonsmooth pitchfork bifurcation diagram of equilibrium points (blue) from the straight motion (black) in the 3D reduced system for $\varepsilon_\psi = 0$ computed by numerical continuation.

Near the bifurcation, $r_\pm \approx 0$ and $r_+ > 0 > r_-$ hold, so that these solutions slowly drift unboundedly parallel to the line of equilibria in opposite directions. Since ψ is an angular variable in the model, for large variations of ψ , the 4D phase space should be viewed as a cylinder. This is consistent with the equations due to the fact that for $\varepsilon_\psi = 0$ the vector field is independent of ψ . On this cylinder, the bifurcating solutions are periodic orbits with winding number ± 1 for $r = r_\pm$, respectively.

On the other hand, at $\varepsilon_\psi = 0$ the linear part A of (3.22) in (3.3) possesses a zero eigenvalue for any ε_r and a double zero eigenvalue at $\varepsilon_r = \varepsilon_{r_1}$ with a 2×2 -Jordan block. The remaining two eigenvalues are negative. The occurrence of the Jordan block suggests that the unfolding contains elements of a symmetric Bogdanov–Takens bifurcation beyond the pitchfork; cf. [5]. Indeed, the stability boundary (3.1) is a curve of Hopf bifurcations in parameter space that will be further studied in the next section. We numerically find global bifurcations in §4, but its rigorous analysis is beyond the scope of this paper. We note that the situation is degenerate by the line of equilibria and the nonsmooth nonlinearity, which already makes the following Hopf bifurcation analysis more involved.

3.3.2 Hopf bifurcations

Consider any control parameters $\varepsilon_r \geq 0$, $\varepsilon_\psi > 0$ on the stability boundary defined by (3.5). Due to Theorem 3.2, the eigenvalues of the linearization at $(u, v, r, \psi) = (u_0, 0, 0, 0)$ consist of one complex conjugate pair with non-zero imaginary parts, and two negative real eigenvalues. Thus, near any such $(\varepsilon_r, \varepsilon_\psi)$, the linear part A of (3.22) can be transformed into a real normal form as a 4×4 -block-diagonal matrix. The blocks from top left to bottom right can be arranged as $\lambda_1 = p_{11} < 0$ from (3.22), a 2×2 -matrix for the complex eigenvalues $\lambda_\pm = \mu \pm i\omega$ with $\omega > 0$, and a real eigenvalue $\lambda_4 < 0$. Due to Theorem 3.2, μ strictly decreases as $\varepsilon_r, \varepsilon_\psi$ cross the stability boundary into the stable region.

In the following, we perform the coordinate changes and identification of terms that allow to apply the theory from [18]. This will then justify to neglect the terms we drop in the coming steps. In particular, since $\lambda_1 < 0$ is already a block of the linear part A from (3.3), the results from [18] imply that we can neglect the first equation of (3.22) for our bifurcation analysis. Therefore, we subsequently analyze the lower right 3×3 -matrix (v, r, ψ) , which contains the linearly oscillating part. We define the matrix $\mathbf{T} = (\mathbf{a}|\mathbf{b}|\mathbf{s})$ with columns $\mathbf{a}, \mathbf{b}, \mathbf{s} \in \mathbb{R}^3$ from the eigenvectors $\zeta_+ = \mathbf{a} + i\mathbf{b}$, $\zeta_- = \mathbf{a} - i\mathbf{b}$, \mathbf{s} , of the eigenvalues $\mu + i\omega$, $\mu - i\omega$, λ_4 , respectively.

Notably, $\mu = 0$ along the curve $\varepsilon_\psi(\varepsilon_r; x_T)$ from (3.10).

Setting $\xi := (\xi_1, \xi_2, \xi_3)^\top = \mathbf{T}^{-1}(v, r, \psi)^\top$, the (v, r, ψ) -subsystem of (3.22) takes the form

$$\begin{pmatrix} \dot{\xi}_1 \\ \dot{\xi}_2 \\ \dot{\xi}_3 \end{pmatrix} = \begin{pmatrix} \mu & -\omega & 0 \\ \omega & \mu & 0 \\ 0 & 0 & \lambda_4 \end{pmatrix} \begin{pmatrix} \xi_1 \\ \xi_2 \\ \xi_3 \end{pmatrix} + h_2(\xi) + \mathcal{R}, \quad (3.25)$$

where $h_2(\xi)$ contains all relevant quadratic-order terms. These have the form

$$h_2(\xi) = \mathbf{T}^{-1} \begin{pmatrix} f_1(\mathbf{T} \cdot \xi) \\ f_2(\mathbf{T} \cdot \xi) \\ 0 \end{pmatrix} = \begin{pmatrix} Z_{11}g_1(\xi) + Z_{12}g_2(\xi) \\ Z_{21}g_1(\xi) + Z_{22}g_2(\xi) \\ Z_{31}g_1(\xi) + Z_{32}g_2(\xi) \end{pmatrix},$$

with quadratic-order functions g_1, g_2 discussed below. Relevant will be the coefficients

$$Z_{11} = \frac{b_2s_3 - b_3s_2}{\det(\mathbf{T})}, \quad Z_{12} = \frac{-b_1s_3 + b_3s_1}{\det(\mathbf{T})}, \quad Z_{21} = \frac{-a_2s_3 + a_3s_2}{\det(\mathbf{T})}, \quad Z_{22} = \frac{a_1s_3 - a_3s_1}{\det(\mathbf{T})},$$

where $a_j, b_j, s_j, j \in \{1, 2, 3\}$ are the components of the vectors $\mathbf{a}, \mathbf{b}, \mathbf{s}$, respectively.

All missing terms are collected in \mathcal{R} , including the nonlinear terms involving u , i.e., $uv, ur, u\psi$, from (3.22), which turn out to be irrelevant at leading-order due to [18, §2, §4]. Furthermore, [18, Thm 2.3] implies that the third component of the transformed system (3.25), ξ_3 , will belong to higher-order terms as well. With these preparations, and using the shorthand $[[\cdot]] := \cdot | \cdot |$ for the second-order modulus terms, the relevant functions g_1, g_2 read

$$\begin{aligned} g_1(\xi_1, \xi_2) &= a_{11}[[a_1\xi_1 + b_1\xi_2]] + a_{12}(a_1\xi_1 + b_1\xi_2)|a_2\xi_1 + b_2\xi_2| \\ &\quad + a_{21}(a_2\xi_1 + b_2\xi_2)|a_1\xi_1 + b_1\xi_2| + a_{22}[[a_2\xi_1 + b_2\xi_2]], \\ g_2(\xi_1, \xi_2) &= b_{11}[[a_1\xi_1 + b_1\xi_2]] + b_{12}(a_1\xi_1 + b_1\xi_2)|a_2\xi_1 + b_2\xi_2| \\ &\quad + b_{21}(a_2\xi_1 + b_2\xi_2)|a_1\xi_1 + b_1\xi_2| + b_{22}[[a_2\xi_1 + b_2\xi_2]]. \end{aligned}$$

At the linear and quadratic-order, the first two equations of (3.25) are independent of ξ_3 such that only these two equations are relevant for the leading-order bifurcation analysis. Setting $(\xi_1, \xi_2) = (\rho \cos \varphi, \rho \sin \varphi)$, these become

$$\begin{cases} \dot{\rho} &= \mu\rho + \chi(\varphi)\rho^2 + \mathcal{O}(\rho^3), \\ \dot{\varphi} &= \omega + \Omega(\varphi)\rho + \mathcal{O}(\rho^2). \end{cases} \quad (3.26)$$

Decisive for the bifurcation is the expression $\chi(\varphi)$, which can be determined using [18, Thm 2.3]. With the abbreviations $c := \cos \varphi, s := \sin \varphi$ and $\Lambda := cZ_{11} + sZ_{21}, \Gamma := cZ_{12} + sZ_{22}$ this gives

$$\begin{aligned} \chi(\varphi) &= (a_{11}\Lambda + b_{11}\Gamma)[[a_1c + b_1s]] + (a_{12}\Lambda + b_{12}\Gamma)(a_1c + b_1s)|a_2c + b_2s| \\ &\quad + (a_{21}\Lambda + b_{21}\Gamma)(a_2c + b_2s)|a_1c + b_1s| + (a_{22}\Lambda + b_{22}\Gamma)[[a_2c + b_2s]]. \end{aligned} \quad (3.27)$$

Before formulating the theorem, we recall the two generic forms of a Hopf bifurcation: in the supercritical (or safe) case the stable fixed point becomes unstable when the stable periodic orbit is created, so that the stable periodic orbit coexist with the unstable equilibrium. In the subcritical (or unsafe) scenario the unstable fixed point becomes stable when an unstable periodic orbit is born. We next show that this criticality is determined by a non-zero sign of

$$\Sigma := \int_0^{2\pi} \chi(\varphi) d\varphi.$$

Here $\chi(\varphi)$ depends on the chosen $\varepsilon_r, \varepsilon_\psi$ on the stability boundary (3.10).

Theorem 3.3. *Let $\varepsilon_\psi > 0$ and $x_T < x_{T_3}$, if $x_{T_2} < x_{T_1}$, or $x_T < x_{T_1}$, if $x_{T_1} < x_{T_2}$; see (3.13). Then, as the control parameter values cross the stability boundary (3.5), the straight motion equilibrium undergoes a Hopf bifurcation which is supercritical if $\Sigma < 0$ and subcritical if $\Sigma > 0$. Furthermore, in terms of the real part μ of the critical eigenvalues, the amplitude of the periodic orbit is given by*

$$\rho = -\frac{2\pi}{\Sigma} \mu + \mathcal{O}(\mu^2). \quad (3.28)$$

Remark 3.4. *The ψ -component of the bifurcating periodic orbits lies in an order μ neighborhood of the equilibrium value $\psi = 0$. Therefore, these solutions have winding number zero in the 4D phase space viewed as a cylinder with ψ from the unit circle.*

Proof. We recall from Theorem 3.2 that the real part μ of a simple complex conjugate pair of eigenvalues crosses the imaginary axis with non-zero derivative as $(\varepsilon_r, \varepsilon_\psi)$ crosses the graph of (3.5). Thus, the equivalent system (3.22) is amenable to [18, Cor. 4.7]. In particular, the non-oscillatory linear part is invertible since $\lambda_1, \lambda_4 < 0$ on the stability boundary by Theorems 3.1 and 3.2. Due to [18, Cor. 4.7], the criticality of the Hopf bifurcation is that of (3.26), and determined by the sign of Σ . Finally, the directly related claimed leading-order amplitude of the bifurcating periodic orbits follows from [18, Prop. 3.8]. \square

The quadratic nonsmooth nature of the nonlinear terms is reflected in the leading-order linear dependence of the amplitude r in (3.28), which would be a square root in the smooth case. This difference to the smooth situation appears also in the unfolding of the pitchfork bifurcation in §3.3.1 with respect to ε_r . Similar to the smooth case, concrete computations of Σ are complicated by the fact that the eigenvectors enter non-trivially. Hence, even with the formula (3.27) and despite the fact that all terms in χ can be explicitly integrated, it appears difficult to determine the sign of Σ analytically.

Nevertheless, numerical evaluation of all these quantities and thus of Σ is highly accurate and almost instantaneous on modern computers. This makes it possible to readily predict the criticality as well as the leading-order expansion of the bifurcating periodic solutions. Rather than Σ , we compute the leading-order dependence of the amplitude in terms of the control parameter ε_r . This gives quantitative insight into the sensitivity of the resulting ship motion in addition to information on the criticality of the bifurcation. Let $(\varepsilon_r^0, \varepsilon_\psi^0)$ denote some chosen

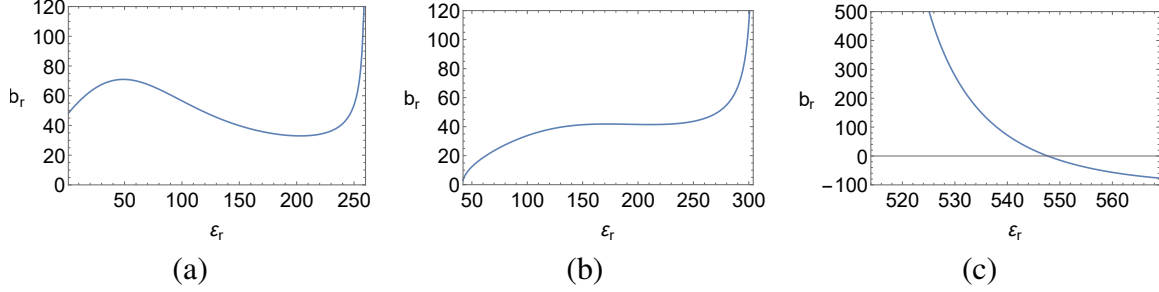


Figure 8: Values of b_r for (a) $\varepsilon_r \in [1, 260]$ in the HTC, see Fig. 6 case 1; (b) $\varepsilon_r \in [42, 304]$ with $x_T = -0.3$, see Fig. 6 case 2; and (c) $\varepsilon_r \in [514, 569]$ with $x_T = 0.16$, case 4 in Fig. 6. The graph in (c) is capped since the b_r values become very large.

control parameters on the stability boundary and set $\tilde{\varepsilon}_r := \varepsilon_r - \varepsilon_r^0$. Expanding (3.28) in terms of $\tilde{\varepsilon}_r$ yields

$$\rho = -b_r \tilde{\varepsilon}_r + \mathcal{O}(\tilde{\varepsilon}_r^2), \quad b_r := \frac{2\pi}{\Sigma} \partial_{\varepsilon_r} \mu(\varepsilon_r^0, \varepsilon_\psi^0), \quad (3.29)$$

which can be evaluated using (3.19). By Theorem 3.2 we know that $\partial_{\varepsilon_r} \mu(\varepsilon_r^0, \varepsilon_\psi^0) < 0$ holds, except to the right of the maximum of the stability boundary in case it has parabolic shape. Hence, b_r has the opposite sign of Σ except in the latter situation. In Fig. 8 (a) we plot the results for the classical HTC, where the stability boundary is monotone. Since $b_r > 0$, the Hopf bifurcation is supercritical for any stabilizing P-control, which means a safe control scenario. The dependence of b_r on ε_r is non-monotone in the interior, but grows significantly and monotone near the right boundary, where ε_ψ tends to zero. As a result, the amplitude of the bifurcating stable periodic orbits is more sensitive to ε_r in this region of the stability boundary.

Concerning changes in the thruster position from the HTC default, we recall from §3.2 that there are four controllable cases as shown in Fig. 6. At $x_T = -0.3$, which is case 2, stabilization by $\varepsilon_\psi > 0$ is possible for approximately $\varepsilon_r \in (41.9, 304.9)$; at $\varepsilon_\psi = 0$ any $\varepsilon_r > 305$ stabilizes the straight motion equilibrium; see Fig. 5 (a). We plot the resulting values of b_r in Fig. 8 (b). Here b_r increases monotonically in ε_r , again with stronger growth near the right boundary, where ε_ψ tends to zero. For $x_T = -0.16$, which corresponds to case 3 in Fig. 6, we omit the plot in which we find a qualitatively reflected b_r graph, so that again the sensitivity is large for small values of ε_ψ on the stability boundary. The results of the last case 4 with $x_T = 0.16$ are plotted in Fig. 8 (c). In this case, the interval $\varepsilon_r \in (514, 569.9)$ of ε_r -values that admit stabilization by ε_ψ is bounded by the zeros of the parabolic shaped stability boundary; see Fig. 3 (c). Its maximum leads to a sign change of b_r , consistent with a supercritical bifurcation on all parts of the boundary. Here ε_ψ is small near both endpoints, but the sensitivity is larger near the left boundary.

4 Numerical Bifurcation Analysis

In this section we present numerical results that corroborate and illustrate the analysis of the previous sections based on implementing the model in the continuation software AUTO [7]. In

this way the stability boundary for the HTC can be computed by numerically tracking the Hopf bifurcation locus. We find that this agrees, up to numerical error, with the analytical prediction (3.5) of Theorem 3.1.

4.1 Continuation of Periodic Solutions

We have employed numerical bifurcation and continuation to compute the periodic orbits that bifurcate from this stability boundary along curves in the $(\varepsilon_r, \varepsilon_\psi)$ -plane for $\varepsilon_\psi > 0$. Confirming the analytically predicted supercritical nature of the Hopf bifurcations, these periodic orbits exist in a region below the stability boundary; see Fig. 2. As shown in §3.3.1, along the ε_r -axis, i.e., for $\varepsilon_\psi = 0$, the Hopf bifurcation is replaced by a supercritical pitchfork bifurcation in the reduced 3D system for u, v, r .

Let $(u_\pm, v_\pm, r_\pm) \in \mathbb{R}^3$ denote the bifurcating equilibria in the 3D reduced system. In the 4D system (3.22), these take the form $\mathbf{v}_\pm(t) = (u_\pm, v_\pm, r_\pm, \psi_\pm(t)) \in \mathbb{R}^4$ with ψ_\pm from (3.24). In §3.3.1 we have identified these as periodic orbits in the 4D phase space viewed as a cylinder at $\varepsilon_\psi = 0$. However, for any $\varepsilon_\psi > 0$, the vector field depends linearly on ψ through the P-control (2.4). This is generally inconsistent for a model with ψ being the yaw angle, i.e., with the cylindrical geometry of the 4D phase space. This can be ignored as long as the solutions under consideration have ψ contained in an interval of length less than 2π . In particular, this is the case in the stability and Hopf bifurcation analysis, where the bifurcating solutions have winding number zero; see Remark 3.4. Nevertheless, since $\psi_\pm(t)$ are unbounded this issue has to be addressed when studying the perturbation of \mathbf{v}_\pm for $\varepsilon_\psi \approx 0$. Therefore, for such a consideration the control law η in (2.4) needs to be made periodic in ψ .

Remark 4.1. *Consider a control that is 2π -periodic in ψ , that equals (2.4) at $\varepsilon_\psi = 0$, and that is smooth in $u, v, r, \psi, \varepsilon_r, \varepsilon_\psi$. Assume that the linearization of the 3D reduced system in (u_\pm, v_\pm, r_\pm) has no eigenvalues on the imaginary axis. (We have numerically verified this for the HTC for all $\varepsilon_r \geq 0$.) We claim that for $0 < \varepsilon_\psi \ll 1$ the corresponding periodic orbits \mathbf{v}_\pm are perturbed to nearby periodic orbits. Indeed, the linearization of (2.5) at each point on \mathbf{v}_\pm has one zero eigenvalue in the direction of the flow and the three eigenvalues of the 3D reduced system. Therefore, the orbit is a compact, normally hyperbolic invariant manifold without boundary, which is structurally stable under perturbations of a parameter.*

For definiteness, we choose to replace the linear ψ -term in the control law by a sinus,

$$\eta = \varepsilon_r r + \varepsilon_\psi \sin(\psi). \quad (4.1)$$

This satisfies the assumptions of Remark 4.1. Since also $\sin'(0) = 1$, we have that the stability boundary, the supercritical nature of the bifurcations and \mathbf{v}_\pm are identical to before. However, this choice introduces the new straight motion equilibria $(u, v, r, \psi) = (u_0, 0, 0, \pm\pi)$, where the ship direction is exactly opposite to the a priori chosen reference direction $\psi = 0$. This choice of η also has an impact on the continuation in ε_r and ε_ψ of the periodic orbits that bifurcate from the Hopf bifurcations on the stability boundary. We numerically found that there is no qualitative change for $\varepsilon_\psi \geq 1$. Here we have chosen 1 as a relative small reference value and will discuss smaller values later. Instead of the sinus we could choose a function that is the

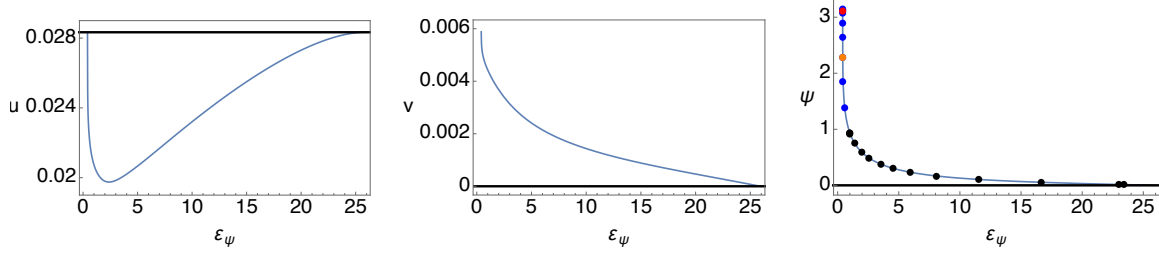


Figure 9: Different views of the global branch of periodic orbits emanating from the (nonsmooth) Hopf bifurcation at $\varepsilon_r \approx 21.2, \varepsilon_\psi \approx 25.9$. At $\varepsilon_\psi \approx 0.408$ the branch appears to terminate in a heteroclinic bifurcation. Plotted are the maximum values of u, v, ψ of the periodic orbits; ψ is in radians. The bullets in the ψ -diagram mark the location of the solutions plotted in Fig. 10: the black bullets are solutions in Fig. 10 (a,b), and the other colors match with the corresponding colored solutions in Fig. 10 (c).

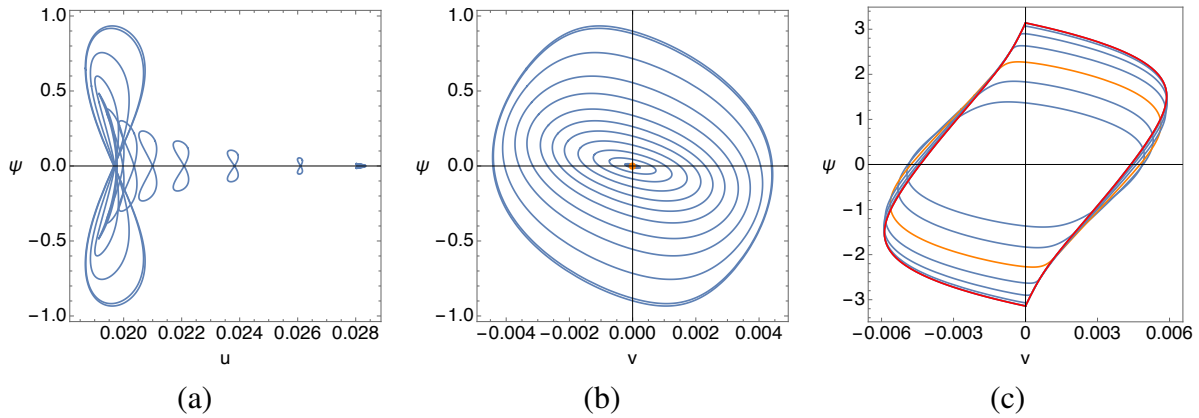


Figure 10: Sample profiles of periodic orbits from Fig. 9. In (a,b) ε_ψ values are between 25.9 at the Hopf bifurcation and $\varepsilon_\psi = 1$. In (c) ε_ψ values are between 1 and the heteroclinic bifurcation point $\varepsilon_\psi \approx 0.408$ with period $T \approx 18570$. ψ is given in radians.

identity for $|\psi|$ below some threshold, but globally smooth and periodic. This would provide results that fully coincide with the P-control as long as $|\psi|$ is below the threshold.

For the sinusoidal control law, we find numerically the presence of a smooth surface of periodic solutions, parameterized by the control parameter values ‘under’ the stability boundary curve within the range $\varepsilon_r \geq 0, \varepsilon_\psi \geq 1$. We have confirmed this along a number of different axis-aligned curves, including the ε_ψ -axis, where $1 \leq \varepsilon_\psi < 45.8$. In Fig. 9 we plot different views of the bifurcation diagram for $\varepsilon_r \approx 21.2$, chosen as an arbitrary non-zero value within the unstable region. This is completely analogous for continuations along different curves. In Fig. 10 we plot some views of periodic solutions on this branch. Similar to the results in [17], we observe a monotone growth of the ψ -range as ε_ψ decreases.

On the one hand, decreasing ε_ψ further, the branch appears to terminate for $\varepsilon_\psi \approx 0.408$ in a heteroclinic bifurcation. It seems that here a heteroclinic cycle exists, which consists of a symmetric pair of heteroclinic orbits between the additional straight motion equilibrium points with $\psi \approx \pm\pi$ rad. Along each of the heteroclinic solutions, the ship direction completes a full

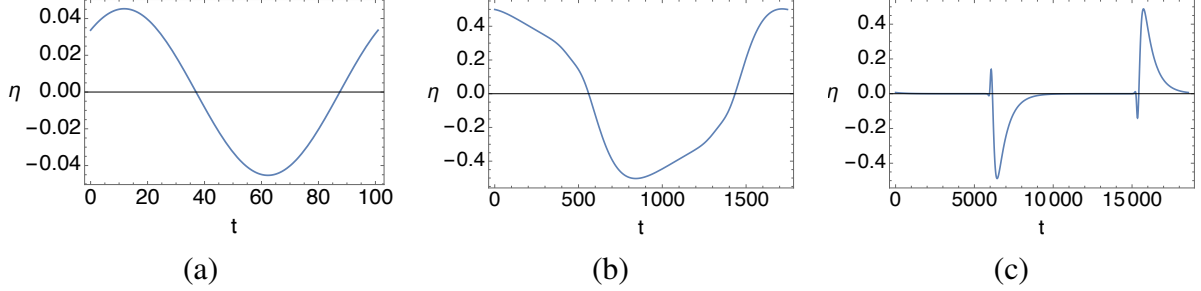


Figure 11: Steering angles $\eta = \varepsilon_r r + \varepsilon_\psi \sin(\psi)$ in radians over one period $t \in [0, T]$ of selected solutions from Fig. 10: (a) $\varepsilon_\psi \approx 25.6$ and $T \approx 101$ (near the origin of Fig. 10 (b)); (b) $\varepsilon_\psi \approx 0.419$ and $T \approx 1747$ (orange in Fig. 10 (c)); (c) $\varepsilon_\psi \approx 0.408$ and $T \approx 18570$ (red in Fig. 10 (c)).

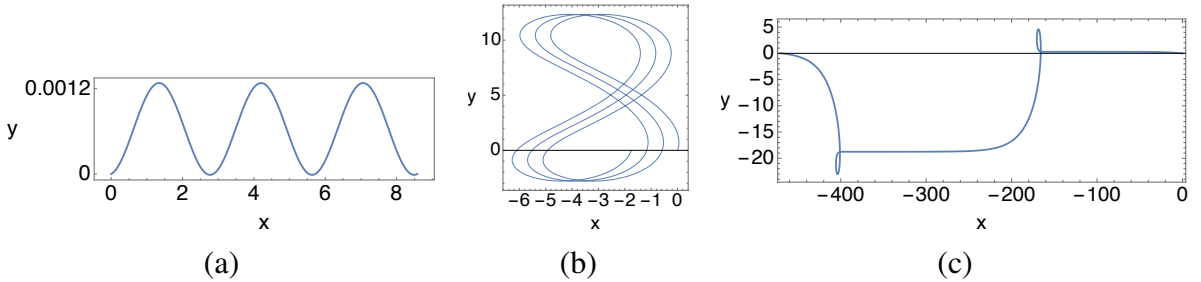


Figure 12: Earth-fixed coordinate plots of the solutions from Fig. 11 (a,b,c), respectively.

circle and asymptotes to the direction opposite to the reference $\psi = 0$. On one of these orbits the rotation is clockwise and on the other it is counter-clockwise. We show one view of a periodic solution near this cycle in Fig. 10 (c) as a red curve.

On the other hand, increasing ε_ψ from zero, we observe that \mathbf{v}_\pm perturb to nearby periodic solutions for $0 < \varepsilon_\psi \ll 1$. This confirms the prediction from Remark 4.1. Further increasing ε_ψ , each of these solutions appears to terminate at $\varepsilon_\psi \approx 0.408$ in one of the heteroclinic orbits that together form the aforementioned heteroclinic cycle. In Fig. 10 (c) this heteroclinic orbit is near one of the parts of the red trajectory with fixed sign of v .

This difference between decreasing and increasing ε_ψ can be understood from the winding numbers of the periodic orbits in the cylinder. The winding number is a homotopy invariant and thus must remain constant along smooth branches. The orbits \mathbf{v}_\pm that bifurcate from $\varepsilon_\psi = 0$ according to Remark 4.1 have winding numbers ± 1 , respectively. Hence, the heteroclinic cycle as a whole has winding number zero, which is compatible with the zero winding number of the periodic orbits that bifurcate from the Hopf points. It appears that this is the way in which the entire region ‘under’ the stability boundary up to the ε_r -axis is organized. We suspect that the heteroclinic cycle and its unfolding can be rigorously studied by analyzing the Bogdanov–Takens-type point at $\varepsilon_\psi = 0$, $\varepsilon_r = \varepsilon_{r_1}$ in the globally cylindrical geometry. In terms of x_T this unfolding might possess additional structure at $x_T = x_{T_-}$, where the stability boundary is vertical, and at $x_T = x_{T_s}$, where the stability region has shrunk to a point; compare Fig. 6.

For further illustration, we plot the steering angle $\eta = \varepsilon_r r + \varepsilon_\psi \sin(\psi)$ of selected periodic solutions in Fig. 11. As expected, for a solution close to the Hopf bifurcation the steering angle

just mildly oscillates. The variations are stronger for solutions that are further from it, but only up to angles of around $0.5 \text{ rad} \approx 28.6^\circ$; cf. Fig. 11 (b,c).

In conclusion, it appears that the bifurcating periodic solutions are confined to the region in parameter space in which the straight motion is unstable. In this region, we find either a periodic orbit with winding number zero, a symmetric pair of periodic orbits with winding number 1 and -1 , or a heteroclinic cycle. We expect that this global arrangement of periodic orbits in parameter space persists for periodic function in (4.1) that are perturbations of the sinus. However, typically there will be quantitative changes, e.g., the additional equilibria will not be exactly opposite to the reference direction $\psi = 0$.

4.2 Periodic Solutions in Earth-Fixed Coordinates

We determine the resulting ship motions in the Earth-fixed position coordinates $(x, y) \in \mathbb{R}^2$. These can be conveniently expressed in complex form as $z = x + iy \in \mathbb{C}$ and the relation of $z(t)$ to a ship-fixed trajectory $(u, v, \psi)(t)$ is given by $\dot{z} = (u + iv) \exp(i\psi)$. An equilibrium point with constant (u, v, ψ) corresponds to the straight motion of the ship if $r = \dot{\psi} = 0$, and to a circular motion if $r = \dot{\psi} \neq 0$. Nevertheless, for periodic solutions $(u, v, \psi)(t)$, the resulting Earth-fixed positions do not need to be periodic.

We plot tracks of Earth-fixed positions for selected solutions from Fig. 10 in Fig. 12. The result for a periodic solution near the Hopf bifurcation is shown in Fig. 12 (a). The equilibrium point involved in the Hopf bifurcation is a straight motion along the x -axis, and the track of the bifurcated periodic solution slightly oscillates about this. The continuation further away from the bifurcation point, e.g., for $\varepsilon_\psi = 1$, results in tracks that oscillate with larger amplitude, but continue to monotonically drift along the x -axis. However, decreasing ε_ψ further, the track turns into a near figure eight shape with self-intersections as shown in Fig. 12 (b); here $\varepsilon_\psi \approx 0.419$. The x -component is non-monotone, but on average there is a drift along the x -axis. Lastly, in Fig. 12 (c) we plot the track along one period of the periodic solution that is close to the heteroclinic cycle mentioned above for $\varepsilon_\psi \approx 0.408$. The track consists of two phases that each resemble one of the heteroclinic orbits involved in the heteroclinic cycle. These heteroclinic orbits are related by reflection and the track also appears to be symmetric about the mid-point between the global y -extrema. The equilibria of the heteroclinic cycle correspond to straight motion opposite to the reference direction. Along the track starting from the right boundary, the ship moves nearly straight along the negative x -axis, and then it makes a clockwise full turn that includes a drift to negative y -values. It continues roughly parallel along the negative x -axis and then turns counter-clockwise with a drift back to near $y = 0$. It appears that this motion repeats periodically.

In conclusion, choosing control gains outside the stability boundary, but not far from it, the resulting ship track still essentially follows the straight heading. For a yaw restoring gain which is not ‘too small’, the ship tracks are also qualitatively unaffected by the alteration of the control law. However, for small $\varepsilon_\psi > 0$ the choice of modification enters into account and, as plotted in Fig. 12 (c), a track occurs which strongly depends on the sinusoidal choice, although the steering angle does not exceed $\pm 29^\circ$.

5 Discussion

We have presented a new method to determine the criticality of Hopf bifurcations for a class of models for ship maneuvering whose nonlinearities contain terms that are continuous but not smooth. This method replaces the smooth theory of center manifolds and normal forms, which is in general not applicable for bifurcations from straight ship motion. As usual in the study of bifurcations, a good understanding of the eigenvalues of the linearization in the underlying steady state is required. For the selected class of models we have therefore performed a detailed analysis of gain margins at which the steady motion changes stability. Here we assumed a standard proportional control for the steering angle that consists of a combination of yaw damping and yaw restoring control. In this study we have been able to identify the geometry of this stability boundary in control parameter space in terms of the ship characteristics. We have shown that the propeller diameter has no qualitative impact, but the position x_T of the propulsion force does. For the HTC characteristics we found that the stable region changes shape at specific locations upon moving x_T further to the fore. More generally, four types of stable regions can occur; in one case the stable region is bounded and otherwise it is unbounded. Stabilization by the chosen control becomes impossible when x_T is larger than an explicit threshold, which is either x_{T_1} or $x_{T_s} < x_{T_1}$ from (3.13). Here $x_{T_1} = N_\beta/Y_\beta$ is a particularly simple ratio of non-dimensional hydrodynamic hull coefficients. In all cases, if the straight motion can be stabilized at all, then this is already possible for zero yaw restoring gain, i.e., $\varepsilon_\psi = 0$.

Our computations of the first Lyapunov coefficient showed that the resulting Andronov–Hopf bifurcations are always supercritical. Also a pitchfork bifurcation that occurs at $\varepsilon_\psi = 0$ is supercritical. Checking this criticality satisfies a request for a nonlinear assessment of stabilizing control from [13]. The supercriticality means that the linear stability boundary can be viewed as a safe prediction for the stabilization of the straight motion equilibrium. As a refinement of this we have simultaneously computed the sensitivity of the amplitude of the bifurcating solutions. We have found that it is more sensitive to the yaw damping gain for small yaw restoring gain, except in the case that the stable region is bounded and the yaw damping is relatively large.

In order to further corroborate that the bifurcating solutions do not interfere with the stabilized course, we have studied the bifurcations more globally using numerical continuation. We found that the bifurcating periodic orbits are indeed fully confined to the region in parameter space where the straight motion is unstable. For the purpose of understanding this organization of solution branches near zero yaw restoring gain, we were forced to modify the proportional control to be periodic in the yaw angle. This modification is not canonical and has an impact on the global behavior of the system. For the specific choice (4.1) we have presented some of the resulting ship tracks. Those for $\varepsilon_r \approx 0$ are strongly affected by this modification, but those for, e.g., $\varepsilon_r \geq 1$ seemed to be qualitatively unaffected.

Towards completing this theoretical study, it would be desirable to unfold the arising double zero eigenvalue point. Challenges are to account for the cylindrical geometry, the non-generic character of the model at $\varepsilon_\psi = 0$, and the nonsmoothness of nonlinear terms.

Concerning the safety of stabilizing the straight motion, it would be interesting to check the criticality of bifurcations in other regimes of ship design parameters, or to change the underlying model. An option would be to consider the more complex rudder model from [22], which we

simplified to the ‘thruster’ model (2.2), or the Ro-Pax ship characteristics and/or the 4 degree-of-freedom model from [17].

Finally, an extension in a different direction would be to move beyond the ship-fixed equilibrium maneuvers and employ numerical continuation to effectively investigate different planned movements. As an example we have the zig-zag maneuvers [21], and the evaluation of so-called overshoots [3].

A HTC Characteristics

The parameter values listed stem from [22]. A part of it can already be found in [21].

Hull forces							
Coeff.	Value	Coeff.	Value	Coeff.	Value	Coeff.	Value
m	0.2328	m_{uu}	0.0247	$X_{u u }$	-0.0141	N_β	-0.1442
I_z	0.0134	m_{vv}	0.2286	Y_β	-0.1735	N_γ	-0.0276
		m_{rr}	0.0150	Y_γ	0.0338	$N_{\beta \beta }$	-0.0375
		m_{vr}	0.0074	$Y_{\beta \beta }$	-1.1378	$N_{\gamma \gamma }$	-0.0386
		m_{rv}	0.0074	$Y_{\gamma \gamma }$	0.0123		
				$Y_{\beta \gamma }$	-0.0537		
				$Y_{ \beta \gamma}$	0.1251		

Table 1: Rescaled added mass coefficients, (2.5), and hydrodynamic bare hull coefficients, (2.2).

Propeller characteristics					
Coeff.	Value	Coeff.	Value	Coeff.	Value
\bar{D}_p	6.105	K_{T0}	0.366897	L_{pp}	153.70
		K_{T1}	-0.345036	T	10.30
		K_{T2}	0.068841	t	0.22
		K_{T3}	-0.710991	w	0.38
		K_{T4}	0.948559		
		K_{T5}	-0.428915		

Table 2: Propeller characteristics with propeller diameter $[\bar{D}_p] = m$, non-dimensional coefficients K_{T_i} of the propeller thrust T_p , corresponding to the model No. 5286., and further parameters: length between perpendiculars $[L_{pp}] = m$, mean draft $[T] = m$, and non-dimensional thrust deduction fraction t and wake fraction w .

Acknowledgments

This research has been supported by the Deutsche Forschungsgemeinschaft (DFG, German Research Foundation), project 281474342/GRK2224/1. We thank Ed van Daalen from MARIN

for initiating this study and sharing reports as well as supporting the initial implementation in AUTO together with the intern Antoine Anceau. We also thank Mathias Temmen for contributing to the initial implementation and linear stability study in the context of his Msc thesis. We are grateful to Thor I. Fossen, from the NTNU, for helpful discussions.

References

- [1] E. H. ABED AND J.-H. FU, *Local feedback stabilization and bifurcation control, I. Hopf bifurcation*, *Systems & Control Letters*, 7 (1986), pp. 11–17, [https://doi.org/10.1016/0167-6911\(86\)90095-2](https://doi.org/10.1016/0167-6911(86)90095-2).
- [2] M. A. ABKOWITZ, *Stability and Motion Control of Ocean Vehicles*, Massachusetts Institute of Technology, MIT, The MIT Press, Printed in the USA, Card Nr. 70-93041, 1969.
- [3] AMERICAN BUREAU OF SHIPPING, *Guide for Vessel Maneuverability*, ABS Plaza, 16855 Northchase Drive, Houston, TX 77060 USA, 2006. Updated February 2017.
- [4] M. APRI, N. BANAGAAYA, J. V. D. BERG, R. BRUSSEE, D. BOURNE, T. FATIMA, F. IRZAL, J. D. M. RADEMACHER, B. RINK, F. VEERMAN, AND S. VERPOORT, *Analysis of a model for ship manoeuvring*, in *Proceedings of the Seventy-ninth European Study Group Mathematics with Industry*, R. Planque, S. Bhulai, J. Hulshof, W. Kager, and R. T.O., eds., Vrije Universiteit Uitgeverij, 2012, pp. 83–116.
- [5] J. CARR, *Applications of centre manifold theory*, vol. 35 of *Applied Mathematical Sciences*, Springer-Verlag, New York-Berlin, 1981.
- [6] G. CHEN, J. L. MOIOLA, AND H. O. WANG, *Bifurcation control: Theories, methods, and applications*, *International Journal of Bifurcation and Chaos*, 10 (2000), pp. 511–548, <https://doi.org/10.1142/S0218127400000360>.
- [7] E. J. DOEDEL, A. R. CHAMPNEYS, T. F. FAIRGRIEVE, Y. A. KUZNETSOV, B. SANDSTEDE, AND X. J. WANG, *Auto97: Software for continuation and bifurcation problems in ordinary differential equations*, Technical report, California Institute of Technology, Pasadena CA 91125, (1998), <http://indy.cs.concordia.ca/auto>.
- [8] T. I. FOSSEN, *Handbook of marine craft hydrodynamics and motion control*, John Wiley & Sons, Ltd., 2011.
- [9] F. R. GANTMACHER, *The Theory of Matrices*, vol. 1, Chelsea Publishing Company, 1960.
- [10] M. GAZOR AND N. SADRI, *Bifurcation controller designs for the generalized cusp plants of Bogdanov–Takens singularity with an application to ship control*, *SIAM Journal on Control and Optimization*, 57 (2019), pp. 2122–2151, <https://doi.org/10.1137/18M1210769>.
- [11] W. KANG, M. XIAO, AND I. A. TALL, *Controllability and local accessibility —a normal form approach*, *IEEE Transactions on Automatic Control*, 48 (2003), pp. 1724–1736.
- [12] F. A. PAPOULIAS, C. A. BATEMAN, AND S. ORNEK, *Dynamic loss of stability in depth control of submersible vehicles*, *Applied Ocean Research*, 17 (1995), pp. 205–216, [https://doi.org/10.1016/0141-1187\(95\)00009-7](https://doi.org/10.1016/0141-1187(95)00009-7).

- [13] F. A. PAPOULIAS AND Z. O. ORAL, *Hopf bifurcations and nonlinear studies of gain margins in path control of marine vehicles*, Applied Ocean Research, 17 (1994), pp. 21–32, [https://doi.org/10.1016/0141-1187\(94\)00016-G](https://doi.org/10.1016/0141-1187(94)00016-G).
- [14] M. SINIBALDI AND G. BULIAN, *Towing simulation in wind through a nonlinear 4-DOF model: Bifurcation analysis and occurrence of fishtailing*, Ocean Engineering, 88 (2014), pp. 366–392, <https://doi.org/10.1016/j.oceaneng.2014.06.007>.
- [15] K. J. SPYROU, *Homoclinic Phenomena in Ship Motions*, Journal of Ship Research, 61 (2017), pp. 107–130, <https://doi.org/10.5957/JOSR.170012>.
- [16] K. J. SPYROU AND J. M. T. THOMPSON, *The nonlinear dynamics of ship motions: a field overview and some recent developments*, The Royal Society, 358 (2000), pp. 1735–1760, <https://doi.org/10.1098/rsta.2000.0613>.
- [17] K. J. SPYROU, I. TIGKAS, AND A. CHATZIS, *Dynamics of a Ship Steering in Wind Revisited*, Journal of Ship Research, 51 (2007), pp. 160–173, <https://doi.org/10.5957/jsr.2007.51.2.160>.
- [18] M. STEINHERR ZAZO AND J. D. RADEMACHER, *Lyapunov coefficients for Hopf bifurcations in systems with piecewise smooth nonlinearity*, SIAM J. Appl. Dyn. Syst., 19 (2020), pp. 2847–2886, <https://doi.org/10.1137/20M1343129>.
- [19] M. TEMMEN, *Analyse der Stabilität und Steuerung eines 3DOF-Schiffskörpers*, master’s thesis, Universität Bremen, March 2019.
- [20] I. TIGKAS AND K. J. SPYROU, *Bifurcation Analysis of Ship Motions in Steep Quartering Seas, Including Hydrodynamic “Memory”*, Springer International Publishing, Cham, 2019, pp. 325–345, https://doi.org/10.1007/978-3-030-00516-0_19.
- [21] S. TOXOPEUS, *Deriving mathematical manoeuvring models for bare ship hulls using viscous flow calculations*, Journal of Marine Science and Technology, 14 (2009), pp. 30–38, <https://doi.org/10.1007/s00773-008-0002-9>.
- [22] S. TOXOPEUS, *Practical Application of Viscous-flow Calculations for the Simulation of Manoeuvring Ships*, PhD thesis, the Maritime Research Institute Netherlands (MARIN), May 2011, <https://repository.tudelft.nl/islandora/object/uuid:eedec62b-60e6-4bf6-ad61-27a6337a536b?collection=research>.
- [23] M. VIALON, S. SUTULO, AND C. GUEDES SOARES, *On the order of polynomial regression models for manoeuvring forces*, IFAC Proceedings Volumes, 45 (2012), pp. 13–18, <https://doi.org/10.3182/20120919-3-IT-2046.00003>.
- [24] K. WOLFF, *Ermittlung der Manövriereigenschaften fünf repräsentativer Schiffstypen mit Hilfe von CPMC-Modellversuchen*, Institut für Schiffbau der Universität Hamburg, 1981. Schriftenreihe Schiffbau.